KEK Proceedings 2015-6
October 2015
R

Proceedings of the Twenty-Second EGS Users' Meeting in Japan

August 3 - 4, 2015.

KEK, Tsukuba, Japan

Edited by

Y. Kirihara, Y. Namito and H. Hirayama

High Energy Accelerator Research Organization

High Energy Accelerator Research Organization (KEK), 2015

KEK Reports are available from:

High Energy Accelerator Research Organization (KEK)
1-1 Oho, Tsukuba-shi
Ibaraki-ken, 305-0801
JAPAN

Phone: +81-29-864-5137
Fax: +81-29-864-4604
E-mail: irdpub@mail.kek.jp
Internet: http://www.kek.jp

FOREWARD

The Twenty-second EGS Users' Meeting in Japan was held at High Energy Accelerator Research Organization (KEK) from August 3 to 4. The meeting has been hosted by the Radiation Science Center. More than 100 participants attended the meeting.

The meeting was divided into two parts. Short course on EGS was held at the first half of the workshop using EGS5 code. In the later half, 9 talks related EGS were presented. The talk covered the wide fields, like the medical application and the calculation of various detector responses *etc.* These talks were very useful to exchange the information between the researchers in the different fields.

Finally, we would like to express our great appreciation to all authors who have prepared manuscript quickly for the publication of this proceedings.

Yoichi Kirihara
Yoshihito Namito
Hideo Hirayama
Radiation Science Center
KEK, High Energy Accelerator Research Organization

CONTENTS

Proposal of efficient irradiation system of small type OSL dosimeter for photon beams between 100 – 2000 keV

H. Okino[1], H. Hayashi[2], K. Takegami[1], N. Kimoto[3], I. Maehata[3], Y. Kanazawa[2], T. Okazaki[4], T. Hashizume[4] and I. Kobayashi[4]

[1] Graduate School of Health Sciences, Tokushima University
Kuramoto-cho 3-18-5, Tokushima, Tokushima 770-8503, Japan
[2] Institute of Biomedical Sciences, Tokushima University Graduate School
Kuramoto-cho 3-18-5, Tokushima, Tokushima 770-8503, Japan
[3] School of Health Sciences, Tokushima University
3-18-5 Kuramoto-cho, Tokushima, Tokushima 770-8503, Japan
[4] Nagase Landauer, LTD.
C22-1 Suwa, Tsukuba, Ibaraki 300-2686, Japan
e-mail: hayashi.hiroaki@tokushima-u.ac.jp

Abstract

Currently, we're studying the basic properties of a small-type OSL dosimeter for direct measurement of patient dose in clinically used X-rays and/or gamma-ray regions. In this paper, we focused attention on the energy regions of several hundred keV. In these energy regions, we should be concerned with the secondary electron equilibration, therefore we proposed a new irradiation system in which detection region was totally covered with a phantom having thicknesses of 1-15 mm. Moreover, we examined the accuracy of our system for practical use.

1. Introduction

Recently, a small-type optically stimulated luminescence dosimeter, named "nanoDot OSL dosimeter", was sold commercially by Landauer Inc. [1,2]. Using this dosimeter, we plan to measure the exposure dose of patients who are undergoing X-ray examination for medical diagnosis. Up to now, basic characteristics of the dosimeter in the diagnostic X-ray region have been measured and many reports have been published [3-6]. On the other hand, only a few studies have been published concerning the nuclear medicine region when applying several hundred keV gamma-rays. Hence, we focused attention on the Monte-Carlo simulation code EGS5 to evaluate the basic properties of the nanoDot OSL dosimeter. The aim of this study is to propose an effective simulation system for the nanoDot OSL dosimeter.

In practice, 661 keV gamma-rays emitted by the decay of ^{137}Cs are usually used in a large irradiation room which has sufficient space not to generate improper scattered rays. From the source the gamma-rays were radiated at a solid angle of 4π. A sufficient irradiation area can achieve secondary electron equilibration [7]. In contrast, the Monte-Carlo simulation can use limited random numbers (photons) with a relatively small irradiation system, therefore it is valuable to construct an efficient irradiation system. To achieve compact irradiation system, the dosimeter should be covered with a high density material as proposed later in this study. The surrounding materials can establish secondary electron equilibration, however the materials may generate additional scattered rays. In this study, we proposed the new irradiation system and evaluate the accuracies of the system in terms of calculation cost and fraction of scattered rays.

2. Materials and Methods

Figure 1 (a) and (b) show schematic drawings of the proposed irradiation system. In this study the detection region corresponding to the dosimeter size (cross-sectional surface of 10 mm × 10 mm and thickness of 2 mm [4-6]) was filled with gas as described later. Air-kerma and absorbed dose in this volume were calculated. The detection region was covered with a phantom having a thickness of "t".

Here, we assumed two different types of phantoms: air with density of 1.00 g/cm^3, and PMMA (polymethylmethacrylate) with density of 1.19 g/cm^3. The PMMA phantom is used to mimic a realistic condition, and the air phantom with density of 1.00 g/cm^3 is ideal for the simulation. In addition, the detection region was filled with gas having a density of 0.001205 g/cm^3, which is the same numerical value as the atmosphere. We used two different materials for the detection region; one is air consisting of C:N:O:Ar = 0.000124:0.755268:0.231781:0.012827, which is defined as fractions by weight, and the other is PMMA consisting of H:C:O: = 0.080541:0.599846:0.319613. Table 1 summarizes the material used in the detection region and the surrounding phantom. We applied three different conditions using the materials mentioned above; "Air/Air" indicates detection region with air (0.001205 g.cm^3) and surrounding phantom with high-dense air (1.00 g/cm^3), "Air/PMMA" is air and PMMA phantom, and "PMMA/PMMA" is low-dense PMMA-gas and PMMA phantom. Theoretically speaking, secondary electron equilibration is achieved between the same materials; namely for the conditions of "Air/Air" and "PMMA/PMMA", but we can't observe these conditions in this experiment. On the other hand, "Air/PMMA" is realistic. In this study, we evaluated the simulation accuracy using "Air/Air" and "PMMA/PMMA", and also evaluated the accuracy of "Air/PMMA".

As shown in Fig.1 (a), we used squared the irradiation field having a length of 2R+W, where R is the range of secondary electrons produced from the interaction between photon and the phantom material, and W is the dosimeter size of 1.0 cm. Using Fig. 2, we explain the methodology for the calculation. Fig. 2 (a) and (b) show the basic concept and energy dependence of stopping power (dE/dx) for air and PMMA [8], respectively. When the electron with energy E_i penetrates the material with thickness of Δt, the energy loss ΔE_i is calculated by $\Delta E_i = dE/dx(E_i) \times \Delta t$. Therefore, R was calculated by summation of Δt until the integrated value of ΔE_i agrees with the

incident energy of E. In this study, Δt is set to be 0.01 cm. For 100-2000 keV photon beams, the size of the irradiation field becomes 1.0×1.0 cm^2 to 4.0×4.0 cm^2.

Theoretically speaking, when the electron equilibration is achieved, absorbed dose (D) is equal to collision kerma (K_{col}). Hence, the accuracy of the proposed system was evaluated by the ratio of D to K_{col}. D is defined as absorbed energy of the detection material (region) divided by the product of detection volume (0.2 cm^3) and density (0.001205 g/cm^3). K_{col} was calculated using the following expression:

$$K_{col} = \int_0^{E_{max}} E \times \Phi_{in}(E) \times \left(\frac{\mu_{en}(E)}{\rho}\right)_{det} \mathrm{dE}, \quad (1)$$

where E_{max} is incident photon energy, the product of $E \times \Phi_{in}(E)$ represents energy fluence at surface of detector region, and $(\mu_{en}(E)/\rho)_{det}$ is the mass energy -absorption coefficient [9].

For the proposed system, a small irradiation field was realized owing to the surrounding phantom. Here, the calculation cost, namely use efficiency of generated photons, is defined by ratio of the number of photons between incident to the detection region and generation. In the simulation, we generate 10^8 photons. Moreover, quality of incident photons was investigated by the fraction of scattered rays described by kerma; namely, collision kerma caused by the secondary photons was divided by that caused by both the primary and secondary photons.

3. Results

By calculation of irradiation field, it was found that phantom thicknesses of more than 1 mm, 5 mm, and 10 mm were necessary to achieve electron equilibration for 100-300 keV, 400-1000 keV, and 1500-2000 keV photons, respectively.

Figure 3 shows the result of D/K_{col} for the proposed system with phantom thicknesses of 1 mm, 5 mm, 10 mm, and 15 mm. The condition values of "Air/Air" and "PMMA/PMMA" are included in the range of 1 ± 0.05. The value of D/K_{col} for condition of "Air/PMMA" is systematically lower than 1, however, they are included in the range between 0.9 and 1.

Figure 4 shows the calculation cost for the condition of "Air/PMMA" for 100-2000 keV photons. Calculation cost becomes 70-90% for 100 keV and approximately 10% for 2000 keV. For 100 keV photons, the calculation costs of 1 mm and 5 mm thicknesses are about 20% larger than those of 10 mm and 15 mm because phantom thickness of 1 mm is sufficient for the 100 keV and additional thickness causes attenuation. Increasing photon energy up to 1000 keV, the differences become small. We determined that proper phantom thickness should be applied based on the photon energy.

Figure 5 shows the fraction of scattered rays for the condition of "Air/PMMA" for 100-2000 keV photons. For the phantom being 1 mm in thickness the fraction of scattered X-rays varies approximately from 1.1% to 1.6% for photon energies from 100 keV to 300 keV. The 5 mm thick phantom varies approximately 2.7% to 4.7% for photon energies from 100 keV to 800 keV. The 10

mm thick phantom varies approximately 3.1% to 6.6% for photon energies from 100 keV to 2000 keV. That of phantom thickness of 15 mm varies approximately 4.3% to 7.3% for photon energies of 100 keV to 2000 keV. As clearly seen in the graph, the thicker the phantom used, the more intense the scattered rays were generated.

4. Discussion

We proposed a new irradiation system for evaluation of basic properties for the small type OSL dosimeter to be used for the nuclear medicine region. In this system, the detection region was totally surrounded by a phantom to establish secondary electron equilibration. At the beginning, we examined the conditions of "Air/Air" and "PMMA/PMMA", and then we checked the ratio of D/K_{col} in order to estimate the accuracy of the system. In theory, D is in total agreement with K_{col}. As shown in Fig. 3 the ratio of D/K_{col} deviated between 1 ± 0.05, we evaluated that the accuracy of our simulation which was approximately 5%. In contrast, the ratio of D/K_{col} for the condition of "Air/PMMA" shows a difference of 10%. This result indicates that our method using a condition of "Air/PMMA" has a possibility to evaluate photon and electron transportation with the accuracy of 10% which is consistent with the accuracies of the simulation.

Calculation cost is presented in Fig. 4. The cost of different phantom thickness show no large differences. It is thought that the phantoms having thickness of 1-15 mm could be used in terms of the calculation cost. However, the fraction of the scattered rays depends strongly on phantom thickness as represented in Fig.5. The fraction was less than 7.5%, and for most of the data about 5%. Therefore if researcher does not consider the effect from scattered rays, the estimated kerma may include the uncertainty of about 5%. Compared with the uncertainty of 10% as described in the above section, the error of 5% is much smaller. A preliminary estimation of this study, we concluded that our method can derive kerma with an accuracy of 10%.

Finally we demonstrate the availability of the proposed method by comparison with other irradiation systems. Figure 6 shows a comparison of irradiation systems between proposed (a) and others ((b) and (c)) under the condition of "Air/Air". In the proposed system, the detection region is totally covered with a phantom, and in the other systems, the detection regions are only partially covered. It is clear from the graph that the D/K_{col} is approximately 90% to 50% compared with the ideal value (100%) when systems (b) and (c) are used. We believe the reason for the low values is that electron equilibrium in lateral directions doesn't occur. In a published paper, in order to achieve electron equilibration at the detector region, it is proposed to place the buildup plate directly in front of the detector [10]. An irradiation system mentioned in a published paper is similar to this system (b) in Fig. 6. The proposed system (b) is considered to be valuable for construction of an efficient experiment, but is not appropriate for simulation.

5. Conclusions

We evaluated the basic characteristics of a small-type OSL dosimeter in the energy region of several hundred keV. The EGS5 code is valuable to carry out this research. In this paper, we proposed a new irradiation system which could efficiently be calculated using the EGS5 code. In

the proposed method, the detection region is totally covered with phantoms having thicknesses of 1-15 mm. Moreover, we estimated the calculation cost and fraction rate of the scattered rays. Then, we evaluated the accuracy of our simulation, which was found to be 10%.

References

[1] Jursinic PA. Characterization of optically stimulated luminescent dosimeters, OSLDs, for clinical dosimetric measurements. Medical Physics. 34(12), 4594-4604, 2007.

[2] Lehmann J, Dunn L, Lye JE et al. Angular dependence of the response of the nanoDot OSLD system for measurements at depth in clinical megavoltage beams. Medial Physics. 41(6), 061712-1-9, 2014.

[3] Reft CS. The energy dependence and dose response of a commercial optically stimulated luminescent detector for kilovoltage photon, megavoltage photon, and electron, proton, and carbon beams. Medical Physics. 36(5), 1690-1699, 2009.

[4] Hayashi H, Nakagawa K, Okino H, Takegami K, Okazaki T, Kobayashi I. High accuracy measurements by consecutive readings of OSL dosimeter. Medical Imaging and Information Sciences. 31(2), 28-34, 2014.

[5] Takegami K, Hayashi H, Okino H, Kimoto N, Maehata I, Kanazawa Y, Tohru O, Kobayashi I. Practical calibration curve of small-type optically stimulated luminescence (OSL) dosimeter for evaluation of entrance-skin dose in the diagnostic X-ray. Radiological Physics and Technology. 8, 286-294, 2015.

[6] Hayashi H, Takegami K, Okino H, Nakagawa K, Okazaki T, Kobayashi I. Procedure to measure angular dependences of personal dosimeters by means of diagnostic X-ray equipment. Medical Imaging and Information Sciences. 32(1), 8-14, 2015.

[7] Faiz M. Khan. The Physics of Radiation Therapy. Lippincott Williams & Wilkins, Philadelphia, 2010.

[8] L. Pages, E. Bertel, H. Joffre et al. Energy Loss Range and Bremsstrahlung Yield for 10-keV to 100-MeV Electrons in Various Elements and Chemical Compounds. Atomic Data 4, 1-27, 1972.

[9] Thomas E. Johnson, Brian K. Birky. Health Physics and Radiological Health. Lippincott

Williams & Wilkins, 2012.

[10] R. Beherens, M. Kowatari and O. Hupe. SECONDARY CHARGED EQUILIBRIUM IN ^{137}Cs AND ^{60}Co REFFERENCE RADIATION FIELDS. Radiation Protection Dosimetry, 2009, Vol. 136, No. 3, pp. 168-175.

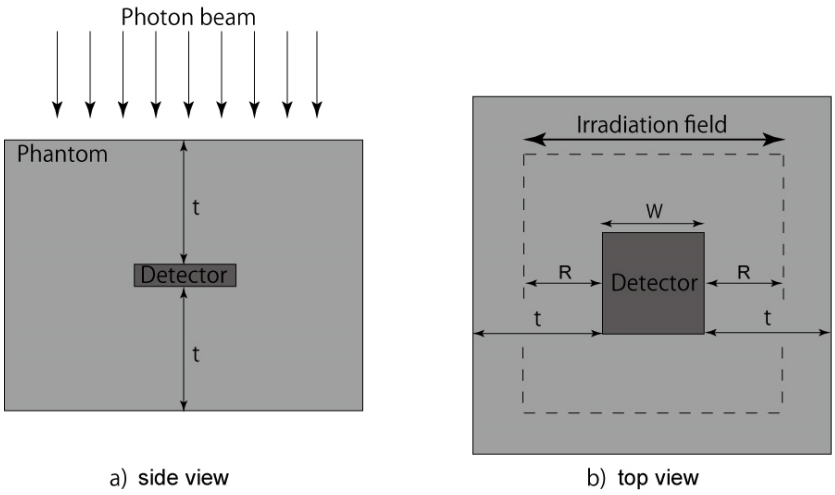

Figure 1. Schematic drawings of the proposed irradiation system.

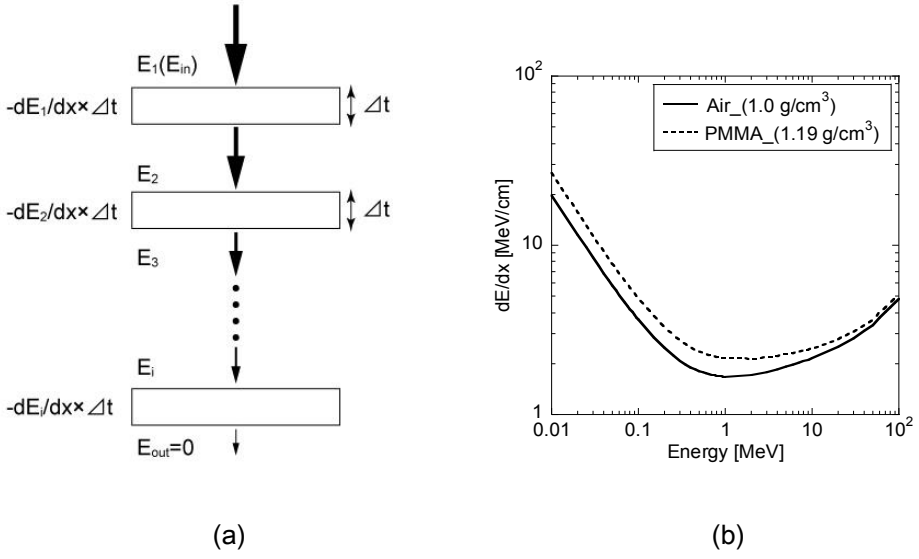

Figure 2. Methodology used to calculate the range of the secondary electron. Figure (a) shows the basic concept of the calculation in which sectional summations were applied. Figure (b) shows energy dependence of dE/dx for air and PMMA.

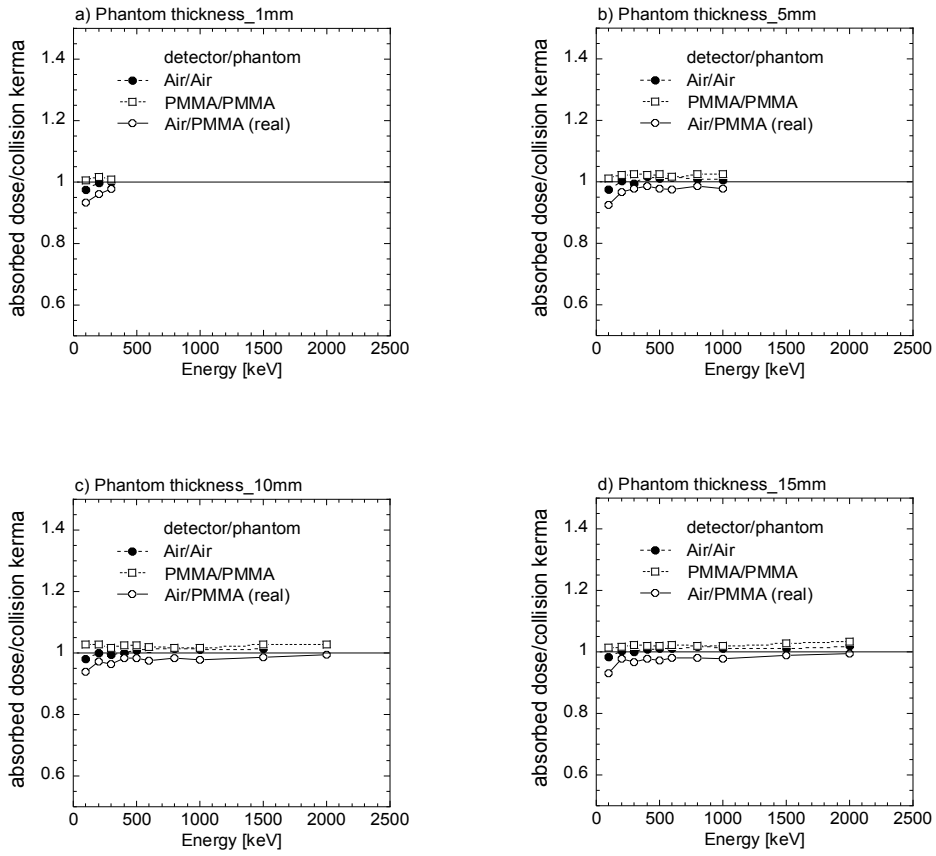

Figure 3. The ratio of absorbed dose and collision kerma as a function of energy. Figures (a), (b), (c) and (d) show the results of t = 1 mm, 5 mm, 10 mm, and 15 mm, respectively.

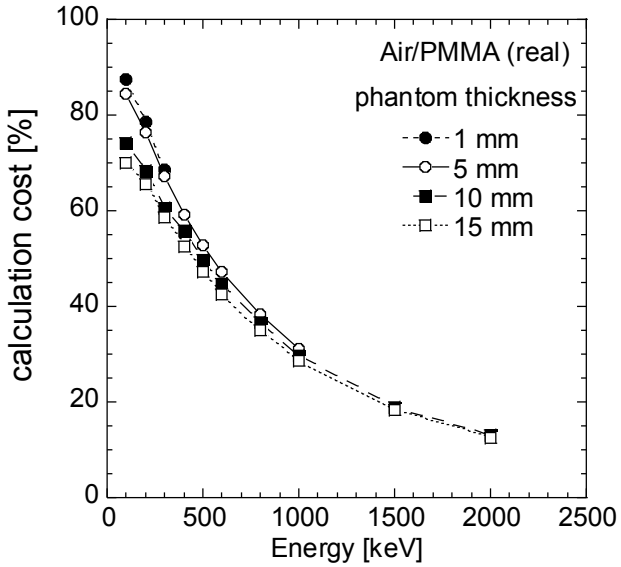

Figure 4. Calculation cost for proposed system.

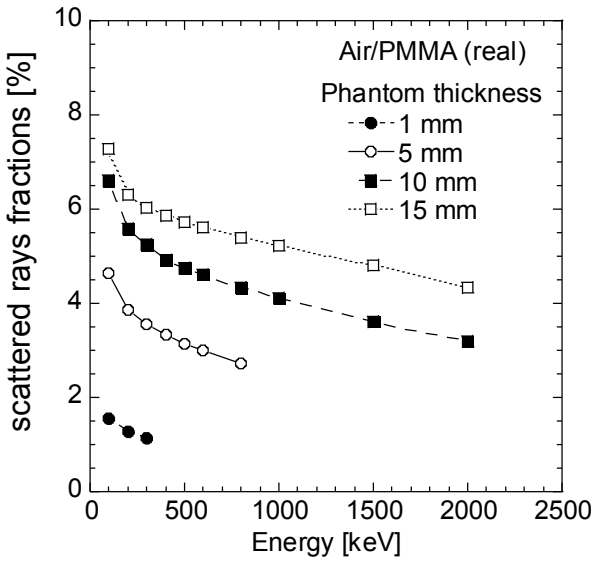

Figure 5. Estimation of the fraction of scattered rays in kerma.

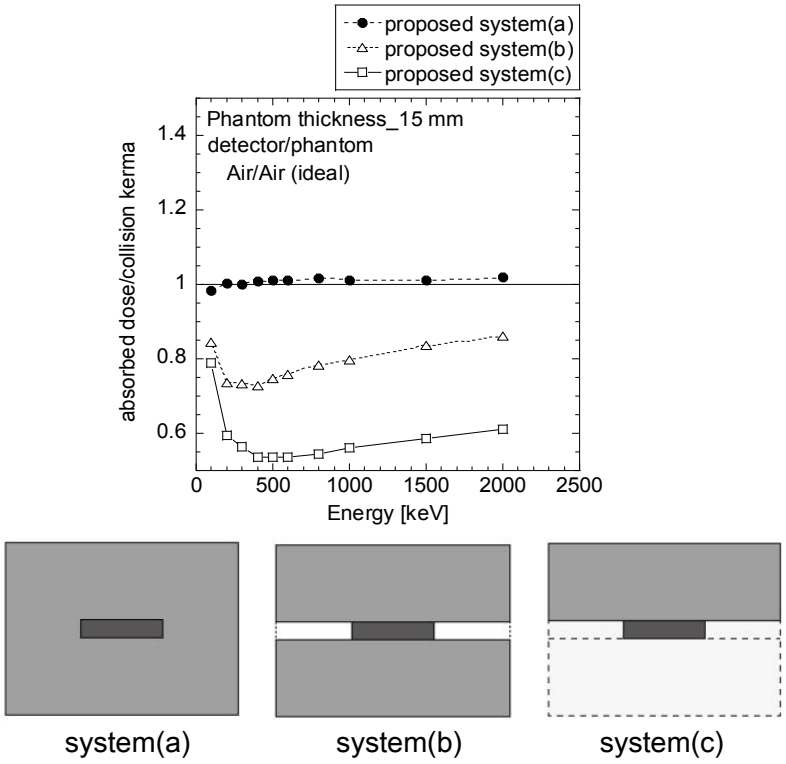

Figure 6. Comparison between our and other systems for the D/K_{col}.

Table 1 Materials used in the detector region and surrounding phantom (see text).

Description (Detector/Phantom)	Detection region		Surrounding phantom	
	Material (Composition*)	Density [g/cm^3]	Material (Composition*)	Density [g/cm^3]
(Air/Air)	C: 0.000124 N: 0.755268 O: 0.231781 Ar: 0.012827	0.001205	C: 0.000124 N: 0.755268 O: 0.231781 Ar: 0.012827	1.0
(Air/PMMA)	C: 0.000124 N: 0.755268 O: 0.231781 Ar: 0.012827	0.001205	H: 0.080541 C: 0.599846 O: 0.319613	1.19
(PMMA/PMMA)	H: 0.080541 C: 0.599846 O: 0.319613	0.001205	H: 0.080541 C: 0.599846 O: 0.319613	1.19

* Numerical values are defined as fractions by weights

Use of Scattered X-Rays for the Estimation of the Attenuation Coefficient

Tetsuya Nakagami, Naohiro Toda, Yoichi Yamazaki, Hiroki Yoshioka, and Shuji Koyama[†]

Information and Computer Sciences, Aichi Prefectural University, Japan

[†]*Nagoya University Brain and Mind Research Center, Japan*

Abstract

In X-ray computed tomography (CT), scattered X-rays are generally removed by a grid located in front of the detector. However, as objects cause the scattered X-rays, information about the objects can be extracted from them. Therefore, using extracted information from the scattered X-rays, the dose to the patient can be reduced. To confirm this assumption, we simplified the reconstruction problem to estimate only one value of the attenuation coefficient.

In this study, we theoretically clarified the principle that the use of a dedicated detector for measuring the scattered X-ray improves the accuracy of the estimated attenuation coefficient according to a simplified model. Furthermore, we confirmed this theoretical insight by conducting a Monte Carlo simulation.

1 Introduction

X-ray computed tomography (CT) is widely used in medical diagnosis, but the radiation dose to which the patient is exposed must be minimized. Grids in front of detectors are used to eliminate the harmful scattered X-rays induced by current X-ray CT devices. However, because objects cause the scattered X-rays, information about the objects can be extracted from them [1].

Given an adequate model of the object, the accurate simulation of the scattering processes yields agreement between virtual projection data and the actual measured projection data. Using a primary scattering model, Kida et al. [2] reconstructed images in a cone-beam CT equipped with a flat-panel detector without grids. We confirmed that an iterative algorithm can prevent harmful influences from the scattered X-rays via a Monte Carlo calculation equipped in EGS5 [3] that performs simulations on an exact multiple-scattering model [1]. However, scattered X-rays may have the potential not only to make grids unnecessary but also to improve the quality of reconstructed images. That is, some exposure reduction can be expected. This aspect has not yet been discussed.

In the present study, by simplifying the problem, we derived a mathematical model to show that the use of scattered X-rays improves the accuracy of the estimated attenuation coefficient. We verified this theoretical insight through numerical experiments.

2 Simplification of the problem

As the target object, a thin water cylinder was exposed to a pencil-beam X-ray. We measured the scattered X-ray photons around the cylinder by using several dedicated ring-shaped detectors (referred to as scatter detectors). The direct X-ray photons were also measured by an ordinary detector, as shown in Figure 1. Our goal was to clarify whether the accuracy was improved by measuring the scattered photons.

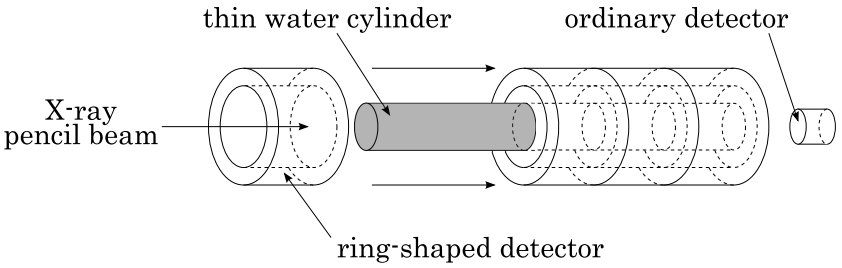

Figure 1: placement of detector

3 Theoretical insight on accuracy of estimation of attenuation coefficient

In this chapter, we present a theoretical insight in the form of an inequality based on a mathematical model.

3.1 T-junction model

The probability that a photon passes directly through the cylinder is $p = \exp(-\mu l)$, where l and μ denote the length and attenuation coefficient of the cylinder, respectively. For simplicity, we assume that all photons that do not pass directly through the cylinder are measured as scattered ones. This situation can be modeled as a T-junction, as shown in Figure 2. For n incident photons, the number $x\,(x \in \{0, 1, \cdots, n\})$ of photons that pass directly through the cylinder is a random variable following a binomial distribution $B(n, p)$ [4]. In the figure, y is a random variable indicating the number of scattered photons $(y = n - x)$.

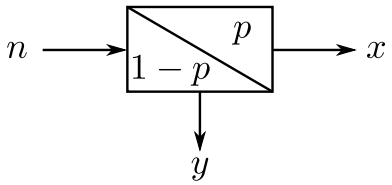

Figure 2: T-junction model

The situation where several scatter detectors are equipped, shown in Figure 1, is modeled by several T-junction models chained in series, as shown in Figure 3. We refer to this model as the k chained T-junction model.

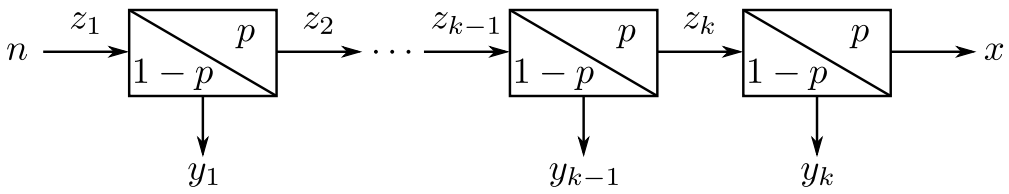

Figure 3: k chained T-junction model

To represent a situation that lacks one scatter detector, we define a model by connecting the last two (k^{th} and $(k-1)^{\text{th}}$) T-junctions shown in Figure 4. In this model, y_k and y_{k-1} are given not separately but together via addition. We refer to this model as the k_{-1} chained T-junction model.

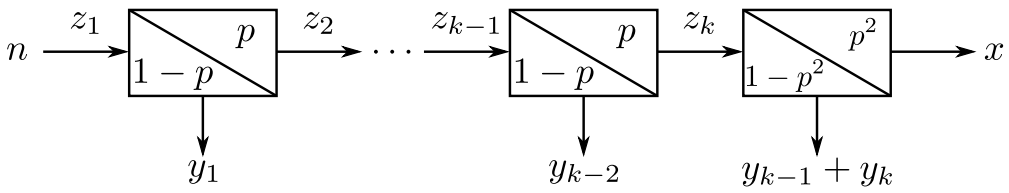

Figure 4: k_{-1} chained T-junction model

3.2 Variance of estimator as a criterion for accuracy

Because the arrival of photons is a stochastic phenomenon, the estimated attenuation coefficients fluctuate randomly. In general, the performance of an estimation method is evaluated by the variance of the estimated parameter. A feature of our problem is that the stochastic structure differs (depending on whether the scattering is measured) between the methods of interest, whereas the number of incident photons is identical. Therefore, we evaluate methods that compare the lower bound of variance of the unbiased estimator. This bound is known as the Cramer Rao lower bound [5] and is expressed as

$$\mathrm{V} = \frac{1}{N \cdot \mathrm{E}\left[\left(\dfrac{\partial}{\partial p}\log\left(f(\boldsymbol{x};p)\right)\right)^2\right]}, \tag{1}$$

where $f(\boldsymbol{x};p)$ is a probability function, $\boldsymbol{x}$ is a random variable, p is the parameter to be estimated corresponding to the attenuation coefficient, and $\mathrm{E}[\cdot]$ denotes the expected value operator. A small value of this bound is preferred. The lower bounds of the k chained T-junction model and the k_{-1} chained T-junction model are denoted as $\mathrm{V}(k)$ and $\mathrm{V}_{-1}(k)$, respectively.

3.3 Improvement of estimation accuracy

Here, we show theoretically that the simultaneous measurement of scattered photons and direct photons improves the accuracy of the estimated parameter and that this effect becomes more conspicuous as the number of scattering detectors increases.

We consider the case of $k = 2$ first. As shown in Figure 5, when x, y_1, and y_2 are given as measured values, the variance of the estimated parameter is defined as $\mathrm{V}(2)$, and as shown in Figure 6, when x and $y_1 + y_2$ are given as measured values, i.e., in the case of one scattering detector, the variance of the estimated parameter is defined as $\mathrm{V}_{-1}(2)$. When only x is given as a measured value, the variance of the estimated value is defined as V_d.

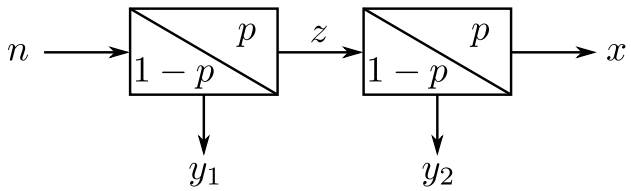

Figure 5: two-chained T-junction model

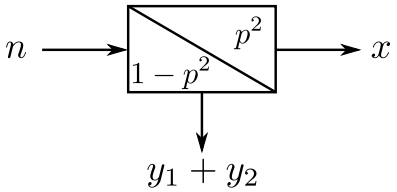

Figure 6: 2_{-1} chained T-junction model

The probability function $f(x, y_1, y_2 \,|\, n, p)$ of the two-chained T-junction model shown in Figure 5 is given as

$$f(y_1, y_2, x \,|\, n, p) = \frac{n!}{y_1!\, x!\, (n - y_1 - x)!} p^{n-y_1+x}(1-p)^{n-x}. \tag{2}$$

Generally, expected value of the function $\phi(y_1, y_2, x)$ is given as

$$\mathrm{E}\left[\phi(y_1, y_2, x)\right] = \sum_{y_1=0}^{n} \sum_{x=0}^{n-y_1} \phi(y_1, y_2, x) f(y_1, y_2, x \,|\, n, p). \tag{3}$$

In our case, substituting $\phi(y_1, y_2, x)$ in the equation (3) by $\left(\dfrac{\partial}{\partial p} \log\left(f(y_1, y_2, x \,|\, n, p)\right)\right)^2$ yields

$$\begin{aligned}
\mathrm{E}\left[\phi(y_1, y_2, x)\right] &= \sum_{y_1=0}^{n} \sum_{x=0}^{n-y_1} \left(\frac{\partial}{\partial p} \log\left(f(y_1, y_2, x \,|\, n, p)\right)\right)^2 \cdot \frac{n!}{y_1!\, x!\, (n - y_1 - x)!} p^{n-y_1+x} (1-p)^{n-x} \\
&= \frac{n^2 - 4n^2 p + 4n^2 p^2}{p^2(1-p)^2} + \frac{2n - 4np}{p^2(1-p)^2} \mathrm{E}\left[x\right] + \frac{1}{p^2(1-p)^2} \mathrm{E}\left[x^2\right] \\
&\quad + \frac{-2n + 6np - 4np^2}{p^2(1-p)^2} \mathrm{E}\left[y_1\right] + \frac{-2 + 2p}{p^2(1-p)^2} \mathrm{E}\left[x y_1\right] + \frac{1 - 2p + p^2}{p^2(1-p)^2} \mathrm{E}\left[y_1^2\right],
\end{aligned} \tag{4}$$

where the expected values are given by

$$\begin{aligned}
\mathrm{E}\left[x\right] &= np^2 \\
\mathrm{E}\left[x^2\right] &= np^2(1 + (n-1)p^2) \\
\mathrm{E}\left[y_1\right] &= n(1-p) \\
\mathrm{E}\left[x y_1\right] &= n(n-1)p^2(1-p^2) \\
\mathrm{E}\left[y_1^2\right] &= n(1-p)(1 + (n-1)(1-p)).
\end{aligned} \tag{5}$$

Therefore, the expected value of the function $\phi(y_1, y_2, x)$ is

$$\mathrm{E}\left[\phi(y_1, y_2, x)\right] = \frac{n(1+p)}{p(1-p)}. \tag{6}$$

On the other hand, the probability function $f(y_1 + y_2, x \,|\, n, p)$ of the 2_{-1} chained T-junction model shown in Figure 6 is given as

$$f(y_1 + y_2, x \,|\, n, p) = \frac{n!}{x!\, (n-x)!} p^{2x} (1-p^2)^{n-x}. \tag{7}$$

The expected value of the function $\phi(y_1 + y_2, x \,|\, n, p)$ becomes

$$\begin{aligned}
\mathrm{E}\left[\phi(y_1 + y_2, x)\right] &= \sum_{x=0}^{n} \left(\frac{\partial}{\partial p} \log\left(f(y_1, y_2, x \,|\, n, p)\right)\right)^2 \cdot \frac{n!}{x!\, (n-x)!} p^{2x} (1-p^2)^{n-x} \\
&= \frac{4n^2 p^2}{p^2(1-p^2)^2} - \frac{8np^2}{p^2(1-p^2)^2} \mathrm{E}\left[x\right] + \frac{4}{p^2(1-p^2)^2} \mathrm{E}\left[x^2\right] \\
&= \frac{4n}{1-p^2}.
\end{aligned} \tag{8}$$

Thus, the variance of the estimated value in each model is given as

$$\mathrm{V}(2) = \frac{p(1-p)}{nN(1+p)}, \quad \mathrm{V}_{-1}(2) = \mathrm{V}_d = \frac{1-p^2}{4nN}. \tag{9}$$

Because we can confirm $\mathrm{V}_{-1}(2) - \mathrm{V}(2) > 0$ easily, the inequality

$$\mathrm{V}(2) < \mathrm{V}_{-1}(2) \tag{10}$$

is derived theoretically. That is, when we use two scatter detectors for measuring the scattered photons, the estimation accuracy of the attenuation coefficient improves.

We next consider the general case of k. $\mathrm{V}(k)$ and $\mathrm{V}_{-1}(k)$ are represented by

$$\begin{aligned} \mathrm{V}(k) &= \frac{p(1-p)^2}{nN(1-p^k)} \\ \mathrm{V}_{-1}(k) &= \frac{(1-p)^2p^3(1+p)}{nN(p^2+p^3-p^k+3p^{k+1}-4p^{k+2})}. \end{aligned} \tag{11}$$

Because

$$\mathrm{V}(k) < \mathrm{V}_{-1}(k) \tag{12}$$

is also derived, we can show that the estimated accuracy of the attenuation coefficient improves when there are many detectors for measuring the scattered X-rays.

4 Numerical experiments

We verified the improvement in the estimation accuracy by performing Monte Carlo simulations for the system shown in Figure 1. The radius of the cylinder is 0.05 cm, the length is 20 cm, and the density is 1.5 times that of water ($\mu = 0.259195$). k ring-shaped NaI scatter detectors are arranged around it. Direct X-rays were measured by an ordinary cylindrical NaI detector with a radius of 0.01 cm and length of 0.1 cm. Furthermore, the X-ray tube, a target object, and an ordinary detector were assumed to be located on a straight line. The number of photons at a single energy of 100 keV was set as 10^5. Because it is difficult to construct an efficient estimator, we employed a maximum-likelihood method using a Monte Carlo simulation with 10^7 photons. We conducted 1,000 experimental trials to estimate the attenuation coefficient, which was evaluated with a mean square error of Err as

$$Err = \sqrt{\frac{1}{N}\sum_{i=1}^{N}(\mu^* - \widehat{\mu}_i)^2}, \tag{13}$$

where N, μ^*, and $\widehat{\mu}$ denote the number of experiments, true attenuation coefficients, and estimated attenuation coefficients, respectively. This criterion includes both bias and variance of the estimated parameter. Here we used specific values of $N = 1000$ and $\mu^* = 0.259195$. We compared the mean square error of two methods: (1) a method based on both scattered and direct X-rays (referred to as the SD method) and (2) a method based on direct X-rays only (referred to as the D method).

The results are shown in Table 1. The improvement in the accuracy as the number of scattering detectors increased is apparent.

Table 1: Simulation result

Method	Number of scatter detector k	Mean $\widehat{\widehat{\mu}}$	Err
D method	–	0.259169	7.111209×10^{-4}
SD method	1	0.259166	7.094014×10^{-4}
	2	0.259198	3.921291×10^{-4}
	10	0.259192	3.584548×10^{-4}

Table 2 shows the results of an example of the exposure-dose reduction for $k = 10$. To obtain the same level of accuracy as the SD method, the D method required 11 times more incident photons. This means that the exposure dose was reduced to approximately 1/11.

Table 2: An example of exposure dose reduction for $k = 10$

Method	Number of incident photons	Mean $\widehat{\widehat{\mu}}$	Err
SD method	10^5	0.259192	3.584548×10^{-4}
D method	10^5	0.259169	7.111209×10^{-4}
	10×10^5	0.259177	3.608225×10^{-4}
	11×10^5	0.259179	3.560456×10^{-4}

5 Conclusions and discussions

In this study, by simplifying the problem, we theoretically showed that the estimation accuracy of the attenuation coefficient can be improved by measuring scattered X-ray photons. A principle to reduce the dose by using scattered X-rays was confirmed. Further theoretical analyses and the development of a CT device employing this principle are required in the future.

References

[1] K. Takemoto, Y. Yamazaki, and N. Toda, "X-ray Computed Tomography Reconstruction using Scattered Radiation", Proc. 20$^{\text{th}}$ EGS User's Meeting in Japan, pp.1–8, 2013.

[2] S. Kida, N. Saotome, A. Haga, Y. Masutai, and K. Nakagawa, "Improvement of Cone-beam CT image quality of radiation therapy", IEICE Technical Report, pp. 417–418, 2012.

[3] H. Hirayama, Y. Namito, A. F. Bielajew, S. J. Wilderman, W. R. Nelson, "The EGS5 Code System, 2005–8, SLAC-R-730", Radiation Science Center Advanced Research Laboratory, High Energy Accelerator Research Organization (KEK), Stanford Linear Accelerator Center, Stanford, CA, 2005.

[4] Patrick Billingsley, "Probability and Measure 3rd ed.", pp. 256, Wiley, New York, ISBN 0-471-00710-2, 1995.

[5] T. Nakamizo, "Signal Analysis and System Identification", pp. 5–7, COLONA PUBLISHING CO., Japan, ISBN 4-339-03081-3, 1995.

A MONTE CARLO SIMULATION BASED ON MEASURED TUBE CURRENT MODULATION DATA IN X-RAY COMPUTED TOMOGRAPHY

M. Inoue[1], S. Koyama[2], T. Haba[1], T. Shibahara[1]

[1]Department of Radiological Technology, Graduate School of Medicine, Nagoya University, 1-1-20 Daiko-Minami, Higashi-ku, Nagoya 461-8673, Japan
[2]Brain and Mind Research Center
1-1-20 Daiko-Minami, Higashi-ku, Nagoya 461-8673, Japan
e-mail: inoue.masaki@a.mbox.nagoya-u.ac.jp

Abstract

In recent times, almost all X-ray computed tomography (CT) scanners use a tube current modulation (TCM) technique. Hence, examining the effects of TCM on the organ doses of patients is very important. To examine the effects of TCM in detail, we have estimated the organ doses in the TCM CT examination using an anthropomorphic phantom and Electron Gamma Shower ver. 5 (EGS5) Monte Carlo simulation. There are some differences between the measurement and simulation results, especially in dosimeters that were inserted near the surface of the phantom. In this study, therefore, we aimed at revealing the reason for differences between measurement and simulations. In the results of this study, it was revealed that the internal dose profile of the patient varies at every scan in helical scanning. In addition, the variance of internal dose profiles increase as the techniques of CT scanning becomes more complicated.

1. Introduction

X-ray computed tomography (CT) is indispensable to medical care for accurate diagnosis. In exchange of high diagnosability, the radiation dose of the X-ray CT examination is much greater than the general radiography examination. To optimize the radiation dose and equalize the image quality, a tube current modulation (TCM) technique was developed. The TCM technique adjusts the X-ray beam intensity over time during scanning in response to the shape or absorption of a patient body. At the beginning of the TCM CT examinations, a topogram that is used to determine the scanning range and the X-ray beam intensity range is acquired. The shape and absorption of the patient body is estimated from the topogram, and the X-ray beam intensity is modulated in response to the shape and absorption data. Because almost all X-ray CT scanners are equipped with the TCM technique now, it is very important to examine the effects of TCM on the organ doses of patients.

To investigate the effects of TCM in detail, we had measured the organ doses using semiconductor dosimeters and estimated the organ doses using Monte Carlo simulation in CT examination. In the measurements, we used an anthropomorphic phantom [Fig.1(a)]. Photodiode dosimeters are inserted at the position of each organ of the anthropomorphic phantom. Using the phantom, we measured the organ doses during whole body helical scanning. In the Monte Carlo simulations, we used Electron Gamma Shower ver.5 (EGS5). To incorporate the changes of the X-ray beam intensity by TCM, we measured the X-ray beam intensity (TCM data) over time during scanning using a small spherical semiconductor dosimeter. Furthermore, we made a voxel phantom that was identical to the anthropomorphic phantom used in the measurements. There were some differences between the measurement and simulation results, especially in dosimeters that were inserted near the surface of the phantom. Because the rotation orbits of an X-ray tube varies at every scan depending on the start time of the irradiation in helical CT scanning, we have estimated that the differences between the measurement and simulation results are because of the differences in the rotation orbits. In this study, we investigated the effect obtained through the differences in the rotation orbits of the measurement and the simulation results.

2. Materials and Methods

2.1 Measurements of the TCM data and the organ doses of the anthropomorphic phantom

We measured the X-ray beam intensity over time during TCM scanning to understand the TCM technique and to introduce the effect obtained by TCM to EGS5. We measured the organ doses of the anthropomorphic phantom that the photodiode dosimeters were inserted at the position of each organ e.g. salivary gland, lung, liver, etc.(1). The measurements are performed with a Discovery CT 750 HD CT scanner (GE Healthcare, Milwaukee, WI, USA) and Brilliance 64 CT scanner (Philips Health Care, Best, the Netherlands) using the general parameters for clinical whole-body scan (tube voltage of 120 kV, beam width of 40 mm, beam pitch of 0.984 in Discovery CT 750 HD, and 0.859 in Brilliance 64). In the Discovery CT 750 HD CT scanner, the TCM system controls the X-ray beam intensity according to the shape of the patient along the long axis, vertical axis, and horizontal axis. On the other hand, in the Brilliance 64 CT scanner, the TCM system controls the X-ray beam intensity according to the shape of the patient only along the long axis. That is the most different parameter between the two CT scanners. For measurement of the TCM data, we used a small spherical semiconductor dosimeter to eliminate of angular dependence [Fig. 1(b)].

First, we acquired the topogram of the anthropomorphic phantom to design a method for modulating the X-ray beam intensity. We then scanned the anthropomorphic phantom according to the designed method and measured the organ doses of the anthropomorphic phantom. Next, we removed the anthropomorphic phantom from bed maintaining the height of the bed. After that, we fixed the spherical dosimeter on the isocenter, and five scans were performed according to the designed methods used for measurement of the organ doses. The five TCM data sets measured at different irradiation-

timings were acquired over time during the whole-body scanning with each CT scanners.

2.2 Estimation of the organ doses using Monte Carlo simulations

The estimations of the organ doses were performed using the EGS5 Monte Carlo simulations. In the simulations, a voxel phantom that simulated the anthropomorphic phantom used in the measurements was incorporated. To simulate the characteristics of the X-ray fan beam, we measured the energy spectra and dose intensities for each angle of the X-ray fan beam, and the energy spectra and dose intensities were incorporated in the Monte Carlo simulation. To simulate the change of X-ray beam intensity, the TCM data were also incorporated in the Monte Carlo simulation. In each CT scanners, we acquired five results using five different TCM data. Then, we discussed in detail the difference of the organ doses between the measurement and simulation results occurred in our previous study.

3. Results

3.1 TCM data

Figure 2 shows the five measurement results of the TCM data in the Discovery CT 750 HD CT scanner and figure 3 shows the same in the Brilliance 64 CT scanner. These TCM data indicated that the X-ray beam intensity cyclically changed over time according to the shape of the anthropomorphic phantom. In addition, we calculated the initial irradiation angle of each measurement using the TCM data. In the Discovery CT 750 HD CT scanner, the initial irradiation angles of the first to fifth measurements were 190.08, 331.2, 232.56, 78.48, and 137.52 degree, respectively. In the Brilliance 64 CT scanner, the initial irradiation angles of the first to fifth measurements were 184.32, 297.36, 16.56, 8.64, and 330.48 degree, respectively.

3.2 Organ doses of the anthropomorphic phantom

Figure 4 shows the measured and calculated organ doses of the anthropomorphic phantom using TCM in the Discovery CT 750 HD CT scanner and figure 5 shows the same in the Brilliance 64 CT scanner. In the Discovery CT 750 HD CT scanner, the maximum variance was approximately 47.6% in the testis and the average variance of all organs was 6.5%. In Brilliance 64 CT scanner, the maximum variance was approximately 31.2% in the salivary gland and the average variance of all organs was 1.8%.

3.3 Dose profiles in a cross section of the anthropomorphic phantom

In the calculation of the organ doses using EGS5, we recorded the absorbed energies of each voxels. To verify the dose profiles of the anthropomorphic phantom visually, the absorbed energies of each voxels were translated to pixel values and the dose profiles were color-coded according to the pixel values using Image J in a cross section of the anthropomorphic phantom. The dose profiles in each CT scanners are shown in figure 6 and figure 7. Although the high-dose areas of the dose profiles

noticeably varied for different scans in the Discovery CT 750 HD CT scanner, the high-dose areas of the dose profiles did not vary much variant in the Brilliance 64 CT scanner.

4. Discussion

In this study, we successfully measured the TCM data in detail over time during scanning using the spherical semiconductor dosimeter. The measured TCM data indicated that the X-ray beam intensity cyclically changed over time according to the shape of the anthropomorphic phantom. We calculated the initial irradiation angles of each scans using these TCM data. In helical CT scanning, when the initial irradiation angles are different, the rotation orbits of the X-ray tube (X-ray beam orbits around the body surface) also varies. Hence, it is thought that the rotation orbits of all the scans were different in this study.

To investigate how the variance of the rotation orbits affects the organ doses, we calculated the organ doses of the anthropomorphic phantom using each TCM data with EGS5. As a result of the calculations, in the Discovery CT 750 HD CT scanner, the variance of organ doses were large especially in testis, salivary gland, and ovary, and the maximum variance was 47.6 % in testis. There were large variances of organ doses near the surface of the phantom. Hence, it is thought that the surface irregularity of irradiation by the difference in the rotation orbits affects the variance of organ doses.

Next, we investigated the internal dose profiles of the anthropomorphic phantom to reveal the reason for small variances during scanning using the Brilliance 64 CT scanner despite differences in their rotation orbits. In the recent X-ray CT scanning, because the X-ray beam spreads widely along the long axis, the X-rays comes from out of across the cross section. The dose profile of the cross section is a combination of all the X-ray contributions including the X-rays come from out of the cross section. In the Brilliance 64 CT scanner, the TCM system controls the X-ray beam intensity only along object's long axis, unless the shape of patients markedly changed in a scanning (e.g. from neck to chest, from chest to abdomen), the X-ray beam intensity hardly changes while the X-ray tube rotates once. On the other hand, in the Discovery CT 750 HD CT scanner, the TCM system controls the X-ray beam intensity according to object's shape along the long axis, vertical axis, and horizontal axis, the intensity of X-ray beam markedly changes while the X-ray tube rotates once. In the three-axis TCM system, therefore, the intensity of the X-rays come from out of the cross section noticeably changes according to start time of the irradiation. This is the reason for variation in the high-dose areas for different measurements using the Discovery CT 750 HD CT scanner.

From the above, it is thought that the variance of internal dose profiles for different scans increases as the X-ray CT scanning technique becomes more complicated. Hence, when we measure the organ doses of a patient only once, there is a possibility that the organ doses are inaccurate. Therefore, we should continue to carefully assess new techniques of X-ray CT scanning and methods of measuring the organ doses of a patient.

5. Conclusions

We acquired the TCM data in detail using the spherical semiconductor dosimeter and performed EGS5 Monte Carlo simulations using the TCM data. As a result, it is revealed that the variance of internal dose profiles for different scans increases as the X-ray CT scanning technique becomes complicated. Hence, we should continue to assess new techniques of X-ray CT scanning and methods of estimating or measuring the patient's dose carefully.

Acknowledgement

This research was supported by grant-in-aid from the Japanese Ministry of Education, Culture, Sports, Science and Technology, (C):26460727 and (C):25350536.

References

1) Takahiko A, Shuji K, Chiyo K. An in-phantom dosimetry system using pin silicon photodiode radiation sensors for measuring organ doses in x-ray CT and other diagnostic radiology, Medical Physics 2002; 29(7): 1504-1510.

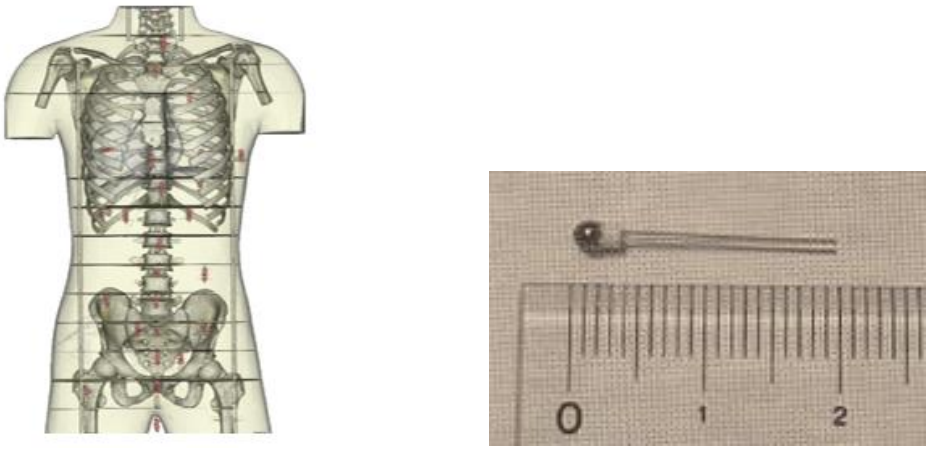

(a) (b)

Figure 1. The anthropomorphic phantom (a) and the sphere semiconductor dosimeter (b)

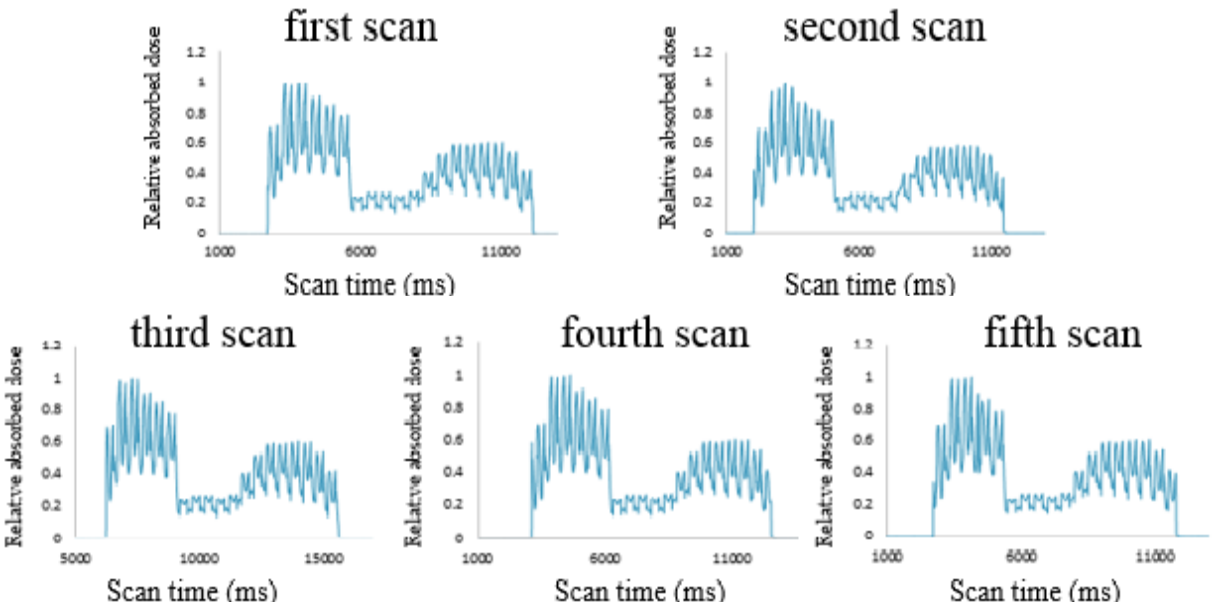

Figure 2. The TCM data measured with the Discovery CT 750 HD CT scanner

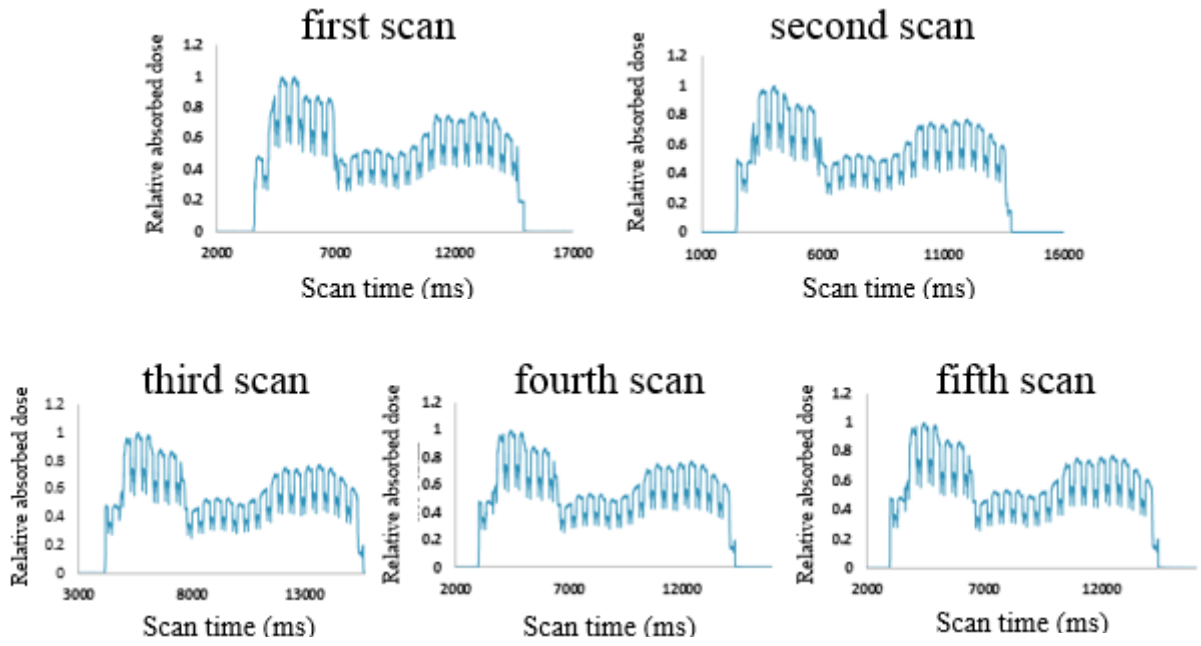

Figure 3. The TCM data measured with the Brilliance 64 CT scanner

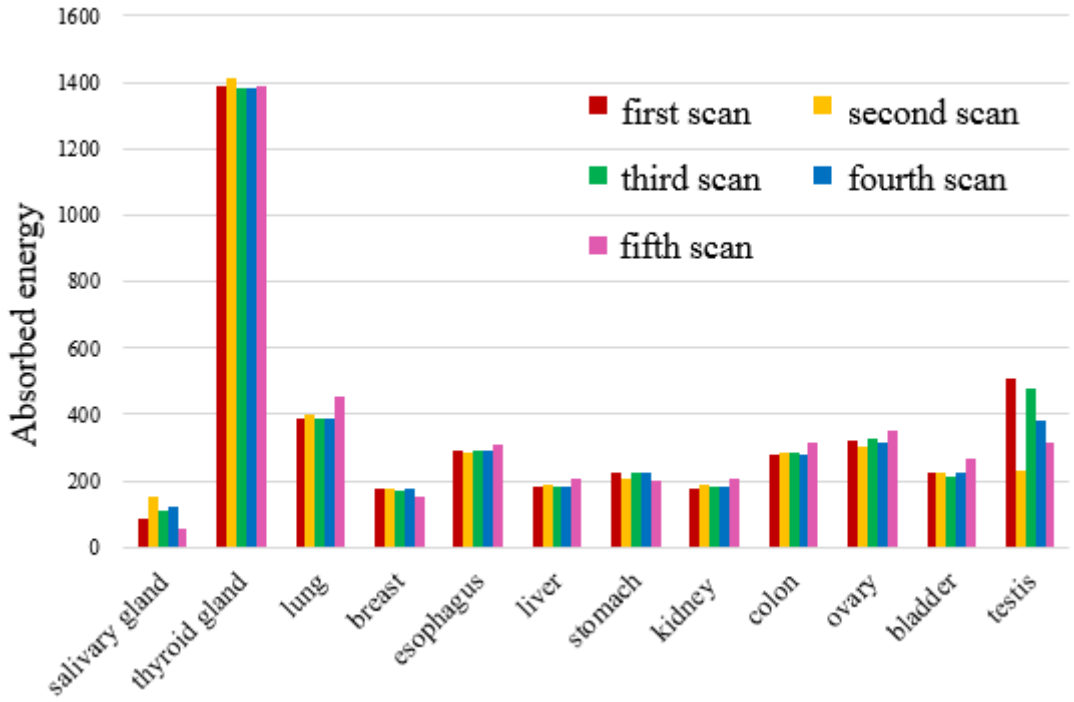

Figure 4. Organ doses of the anthropomorphic phantom measured with the Discovery CT 750 HD CT scanner

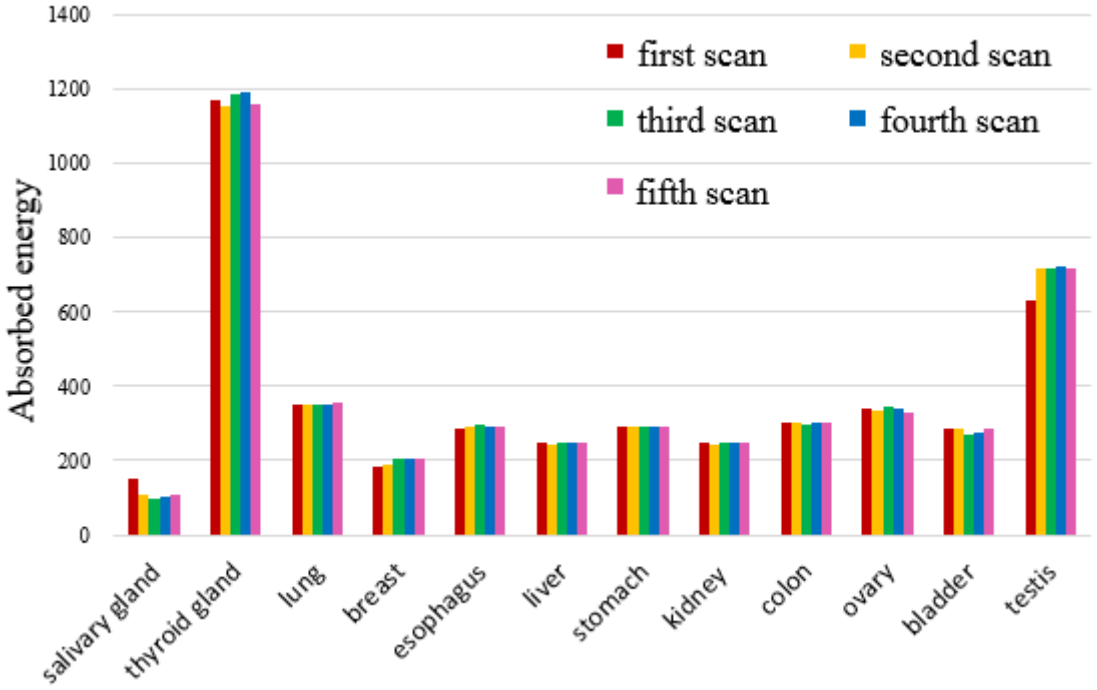

Figure 5. Organ doses of the anthropomorphic phantom measured with the Brilliance 64 CT scanner

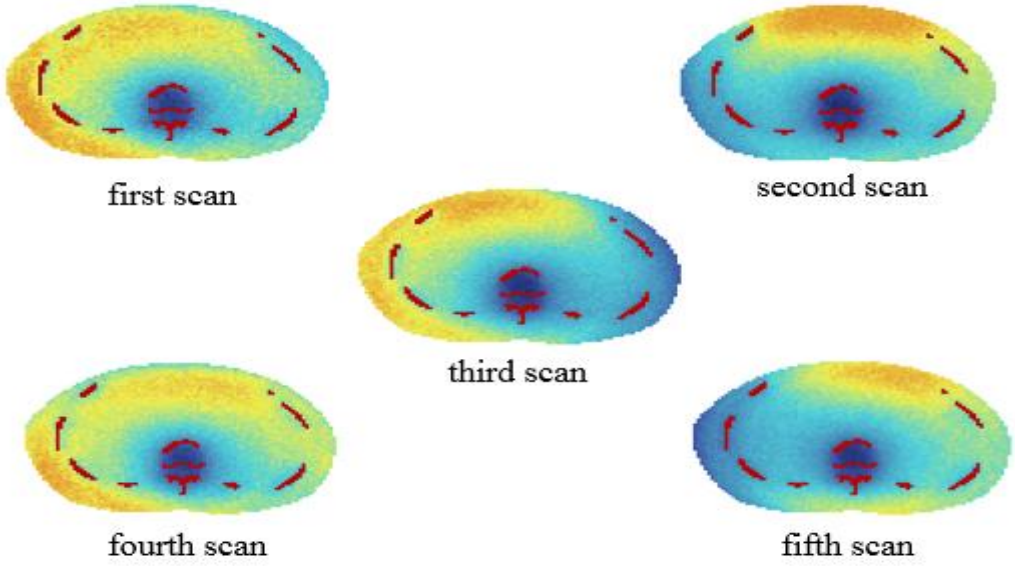

Figure 6. Dose profiles of a cross section in Discovery CT 750 HD CT scanner

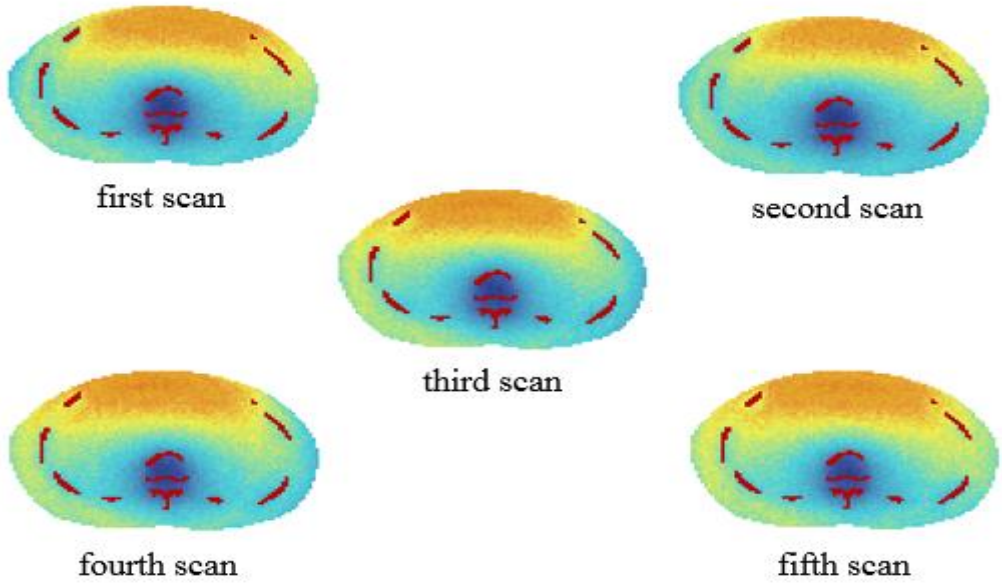

Figure 7. Dose profiles of a cross section in Brilliance 64 CT scanner

RELATIONSHIP BETWEEN THE TUBE VOLTAGE DEPENDENCE OF CROSS-SECTIONAL ABSORBED PROFILE AND EXPOSED DOSE OF SUPERFICIAL RADIOSENSITIVE ORGANS

T. Shibahara[1], S. Koyama[2], M. Inoue[1], T. Haba[3]

[1]Department of Radiological Technology, Graduate School of Medical, Nagoya University
1-1-20 Daiko-Minami, Higashi-ku, Nagoya 461-8673, Japan
[2]Brain & Mind Research Center
1-1-20 Daiko-Minami, Higashi-ku, Nagoya 461-8673, Japan
[3]Radiology and Radiation Oncology, Fujita Health University Hospital
1-98 Dengakugakubo, Kutsukake-cho, Toyoake, Aichi 470-1192, Japan
e-mail: shibahara.tomoki @a.mbox.nagoya-u.ac.jp

Abstract

There has been a growing concern regarding exposure to superficial radiosensitive organs with the rapid increase of computed tomography examinations. Manufacturers have been developing various dose reduction methods in order to prevent harm to these organs. Our previous study revealed a unique phenomenon in X-ray computed tomography scanning, in which the maximum absorbed dose position shifts to a deeper region from the surface in a water cylindrical phantom. We considered that this result could be applied as a dose reduction method. Therefore, in this study, we investigate the tube voltage dependence of this unique phenomenon. The results show that the peak dose position shifts to a deeper region with increasing tube voltage. The superficial radiosensitive organs can thus be protected from peak dose exposure by adjusting the tube voltage.

1. Introduction

X-ray computed tomography (CT) technology is being increasingly used because of the rapid development it has undergone recently, X-ray CT examinations are therefore now the main source of medical radiation exposure globally. Therefore, there is a growing need to reduce the radiation dose to organs, especially superficial radiosensitive organs (such as the lens of the eye, thyroid gland, and breasts) that are directly exposed to the primary X-rays and therefore have higher risks of harm. Various dose reduction methods have been considered, such as: (a) placing a plate composed of bismuth mainly over the organ to attenuate the primary X-ray before deliver to the organ and (b) decreasing the tube current for a range the primary X-ray enter superficial radiosensitive organs over the anterior surface of patient. These techniques use applications such as XCare (Siemense Healthcare, Muenchen, Bayern, Germany) and Organ Dose Modulation (GE Healthcare, Milwaukee, WI, USA).

In a previous study, we obtained the absorbed dose profile in a cylindrical water phantom in two

ways: measurements using a small photodiode, and calculations performed using Monte Carlo simulation (Electron Gamma Shower ver.5; EGS5). A unique phenomenon was observed in the results, in that the maximum dose position shifted to deeper region from the surface of the phantom, as shown in Fig. 1. In other words, organs at the surface, such as the above-mentioned superficial radiosensitive organs, are protected from exposure to the maximum dose. However, the effects of examination parameters on this unique phenomenon remain unclear. In this study, we focus on the tube voltage dependence of this unique phenomenon and apply it for reducing the dose to superficial radiosensitive organs.

2. Materials and Methods

2.1 Measurement of the absorbed dose profile

In our previous study, we measured the absorbed dose profiles in X-ray CT scanning (general abdominal examination; tube current of 200mA, tube voltage of 120kV) by using a small photodiode dosimeter placed in a cylindrical water phantom made by hollowing styrene foam (Fig. 2a). The dosimeter measurements had a sensitive area of 2.8 × 2.8 mm^2, and consisted of a set of pin silicon photodiodes pasted back to back so as to obtain a uniform detection efficiency without angular dependence (Fig. 2b).

2.2 Simulation geometry and condition to obtain the absorbed dose profile

The calculations were performed using the EGS5 Monte Carlo simulation code. We set the geometry to match the abovementioned measurement geometry, as shown in Fig. 3a. The diameter and length of the phantom was 320 and 450 mm, respectively. The scan range was set to a central 100 mm region of the phantom, and the distance from the X-ray focus to the central axis of the phantom (FCD) was 600 mm.

In X-ray CT, the dose profiles and energy spectra of the X-ray fan beam are different for each fan beam angle, because the photons pass through a beam-shaping-filter that has a bowtie-shaped cross section. The dose profiles and effective energies for each fan beam angle were measured for an X-ray fan beam of a CT scanner (AquilionONE, Toshiba Medical Systems Corporation, Tochigi, Japan). The effective energies were converted to energy spectra at each beam angle using Tucker approximation algorithms. These data of the beam-shaping-filter should be incorporated into the simulation. We obtained these data for various tube voltages: 80, 100, 120, and 135 kV. We modified the data for use in the simulation in order to imitate to change tube voltage in CT scanning. The dose was deposited in 320 voxels (10 × 10 × 10 mm^3) lined up in the height direction in the central slice of the phantom, as shown Fig. 3b. In all the calculations, the dose depositions by the scattering x-ray (mainly Compton) and the primary x-ray were evaluated separately. The statistical error for the calculation in the center voxel of the phantom was less than 1.0 %.

3. Results

Figure 4 shows the absorbed dose profiles in the central slice of the cylindrical water phantom in X-ray CT scanning for different tube voltages: (a) 80, (b) 100, (c) 120, and (d) 135 kV. The absorbed dose at each depth was normalized by the dose at the surface of the phantom upper end (320 mm from the phantom lower end on the horizontal axis of the figure). Although the tube voltage was varied, the

unique phenomenon was similarly observed, in that the maximum dose position shifted to a deeper region from the surface of the phantom. At higher tube voltages, the scattering X-ray component and the ratio of the phantom center dose to the surface dose both increased in the dose profile.

Figure 5 shows a comparison of the total absorbed dose profiles for each tube voltage; the data were normalized by (a) the total photon number and (b) the dose of the phantom center. The depth of the maximum dose position at tube voltages of 80, 100, 120, and 135 kV was 11, 15, 18 and 19 mm from the phantom upper end surface, respectively. There was a difference of 8 mm in between voltages of 80 kV and 135 kV. At higher tube voltages, the maximum dose position was deeper from the surface of the phantom.

Figure 6 shows a comparison of the absorbed dose profile caused by (a) the scattering x-ray and (b) the primary x-ray separately at each tube voltage; the data were normalized by the dose at the upper end surface of the phantom. In the primary X-ray component, the difference in the dose profile among each tube voltage was extremely small. Therefore, the unique phenomenon was considered to be mainly caused by the scattering X-ray component.

4. Discussion

The present study, results show that at higher the tube voltages, the maximum absorbed dose position shifts to a deeper region in the phantom. This dependence is considered to be due to the increase in the scattering component with the tube voltage was set higher. In addition, the absorbed dose relatively decreases in the shallow regions of the phantom, where superficial radiosensitive organs are assumed exist. We can thus assume that X-ray CT scanning at higher tube voltages is preferable for protecting superficial radiosensitive organs to lower tube voltage.

In April 2011, the International Commission on Radiological Protection (ICRP) lowered the equivalent dose limit of the lens (occupational dose). In recent studies, threshold dose of cataract formation has been shown to be lower than that adopted previously. Therefore, the reduction dose of the lens has attracted considerable global research interest. In general, for head CT scanning, a low tube voltage, mostly 80 kV, is used in order to increase the contrast of the white and gray matter. However, the present study reveals that the depth of the lens from the surface (approximately 8mm) is roughly matched with the maximum absorbed dose position in CT scanning at 80 kV. If the tube voltage is set 135 kV, the lens can avoid maximum dose, but this will result in a decrease in contrast. Therefore, we should be more careful while setting the tube voltage, considering the balance of the lens dose and the image contrast in head CT.

The limitation of this study is that image quality was not considered. As the relationship between the exposed dose and image quality is a trade-off, we will conduct comprehensive future studies by taking image quality into consideration.

5. Conclusions

This study revealed the tube voltage dependence of the unique phenomenon found in a previous study, in which the maximum absorbed dose position shifts to deeper region from the phantom surface. This phenomenon is observed at any tube voltage, and the maximum absorbed dose position shifts to deeper regions with increasing tube voltage. The fact that the peak dose position shifts to deeper region

indicates that the superficial radiosensitive organs (e.g., lens of the eye, the thyroid gland, and breasts) are protected from unnecessary exposure. Since this method benefits only from a change in the scan parameter, we can combine this method with other dose reduction methods such as Bismuth shield, XCare, or Organ Dose Modulation. This study suggests that the tube voltage dependence could be applied to clinical examination as a beneficial dose reduction method.

Acknowledgment

This research was supported by grant-in-aid from the Japanese Ministry of Education, Culture, Sports, Science and Technology, (C):26460727 and (C):25350536.

References

1) Tomonobu H, Shuji K, Yoshihiro I, "Influence of difference in cross-sectional dose profile in a CTDI phantom on X-ray CT dose estimation: a Monte Carlo study," Radiol Phys Technol, 7, 133-140 (2014).
2) Takahiro A, Shuji K, Chiyo K, "An in-phantom dosimetry system using pin photodiode radiation sensors for measuring organ doses in x-ray CT and other diagnostic radiology," Medical Physics, 29(7), 1504-1510 (2002).
3) Jia W, Xinhui D, Jodie A, Shuai L, Katharine L, Cynthia H, "Bismuth Shielding, Organ-based Tube Current Modulation, and Global Reduction of Tube Current for Dose Reduction to the Eye at Head CT," Radiology, 262(1), 191-198 (2012)
4) Xinhui D, Jia W, Jodie A, Shuai L, Katharine L, Cynthia H, "Dose Reduction to Anterior Surfaces With Organ-Based Tube-Current Modeulation:Evaluation of Performance in a Phantom Study," AJR, 197, 689-695 (2011)
5) C Yamauchi-Kawaura, M Yamauchi, K Imai, T Aoyama, M Ikeda, " IMAGE QUALITY AGE-SPECIFIC DOSE ESTIMATION IN HEAD AND CHEST CT EZAMINATIONS WITH ORGAN-BASED TUBE-CURRENT MODULATION," Radiation Protection Dosimetry, 1-13 (2013)
6) International Commission on Radiological Protection, "Managing patient dose in computed tomography," ICRP Publication 87, Elsevier ICRP (2000)

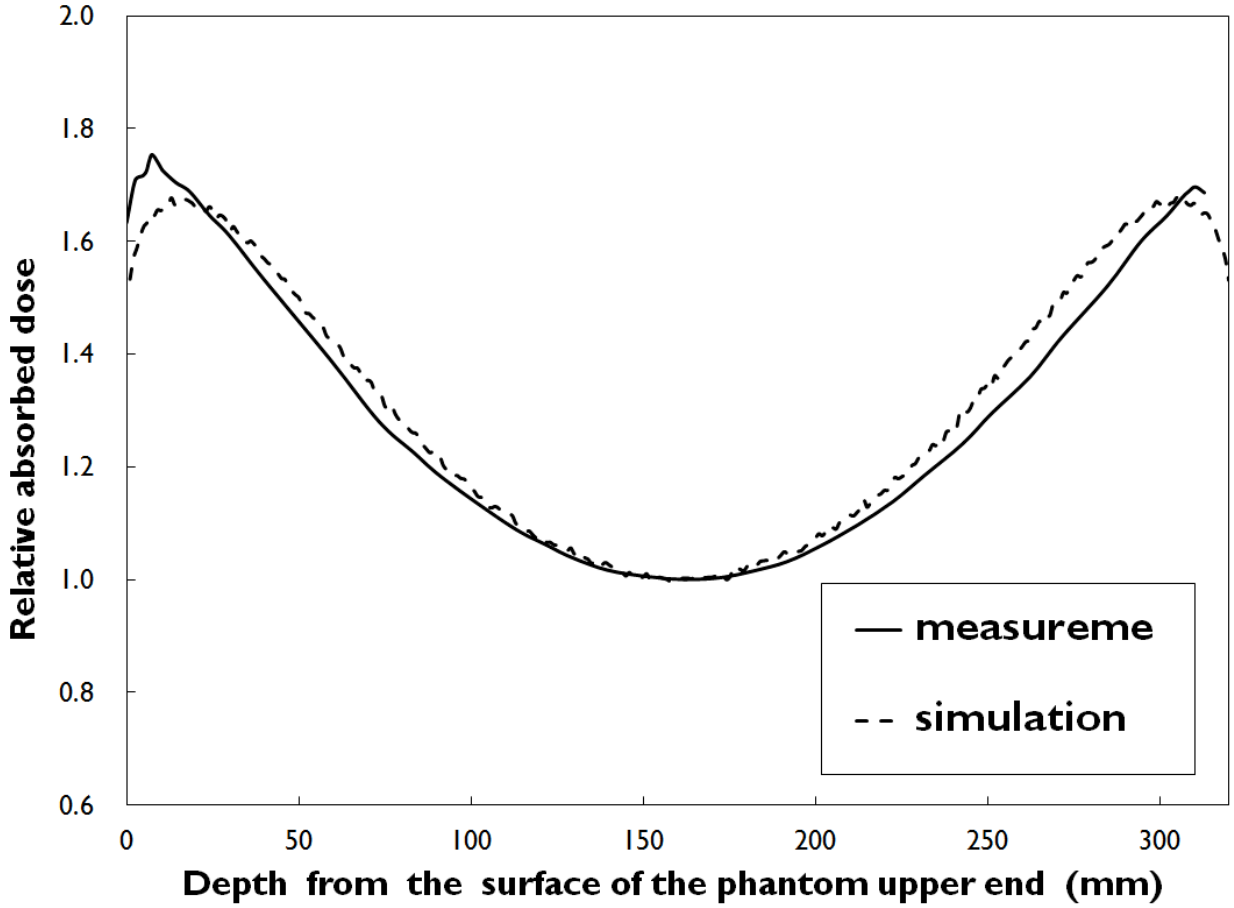

Fig. 1 The measured and simulated absorbed dose profile

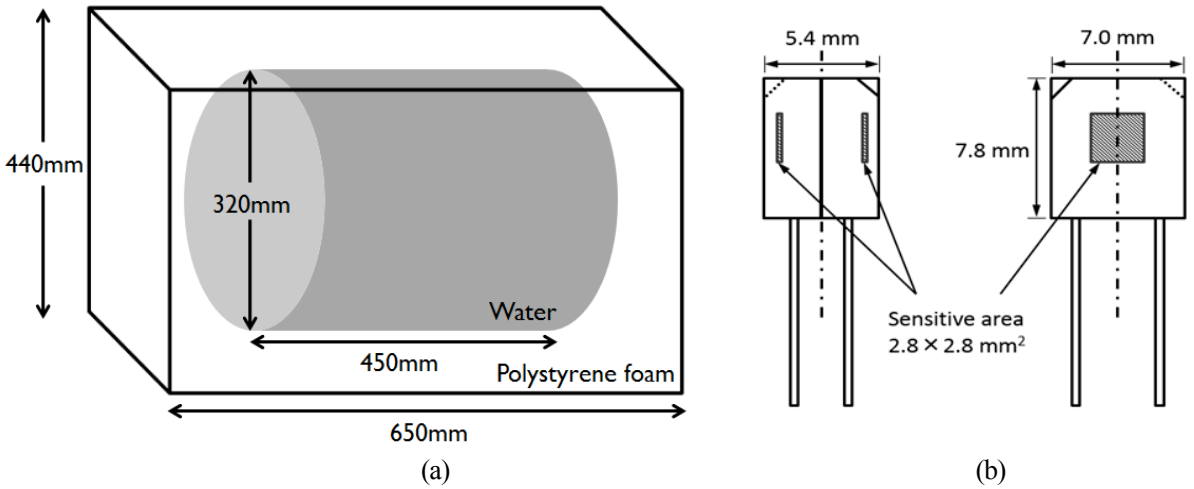

(a) (b)

Fig. 2 (a) The cylindrical water phantom and (b) the photodiode dosimeter

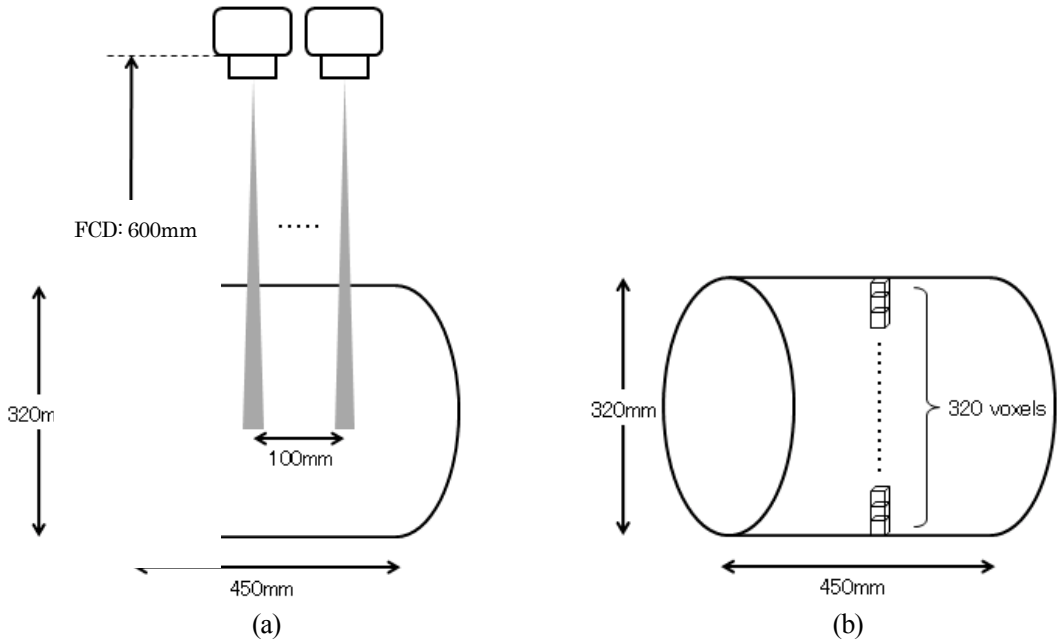

Fig. 3 (a) Simulation geometry and (b) arrangement of voxels to deposit dose

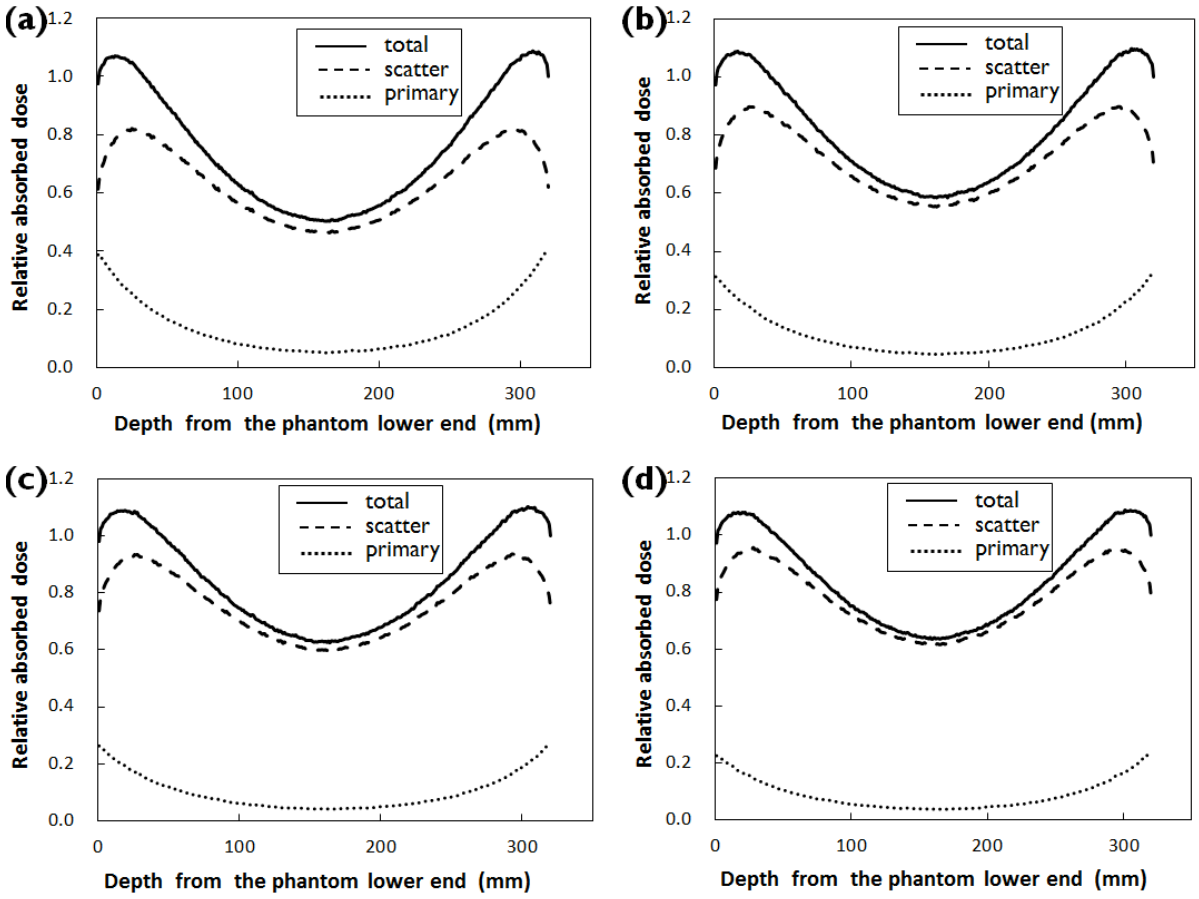

Fig. 4 The absorbed dose profiles in the cylindrical water phantom in the CT scanning varying the tube voltage; (a) 80, (b) 100, (c) 120 and (d) 135 kV.

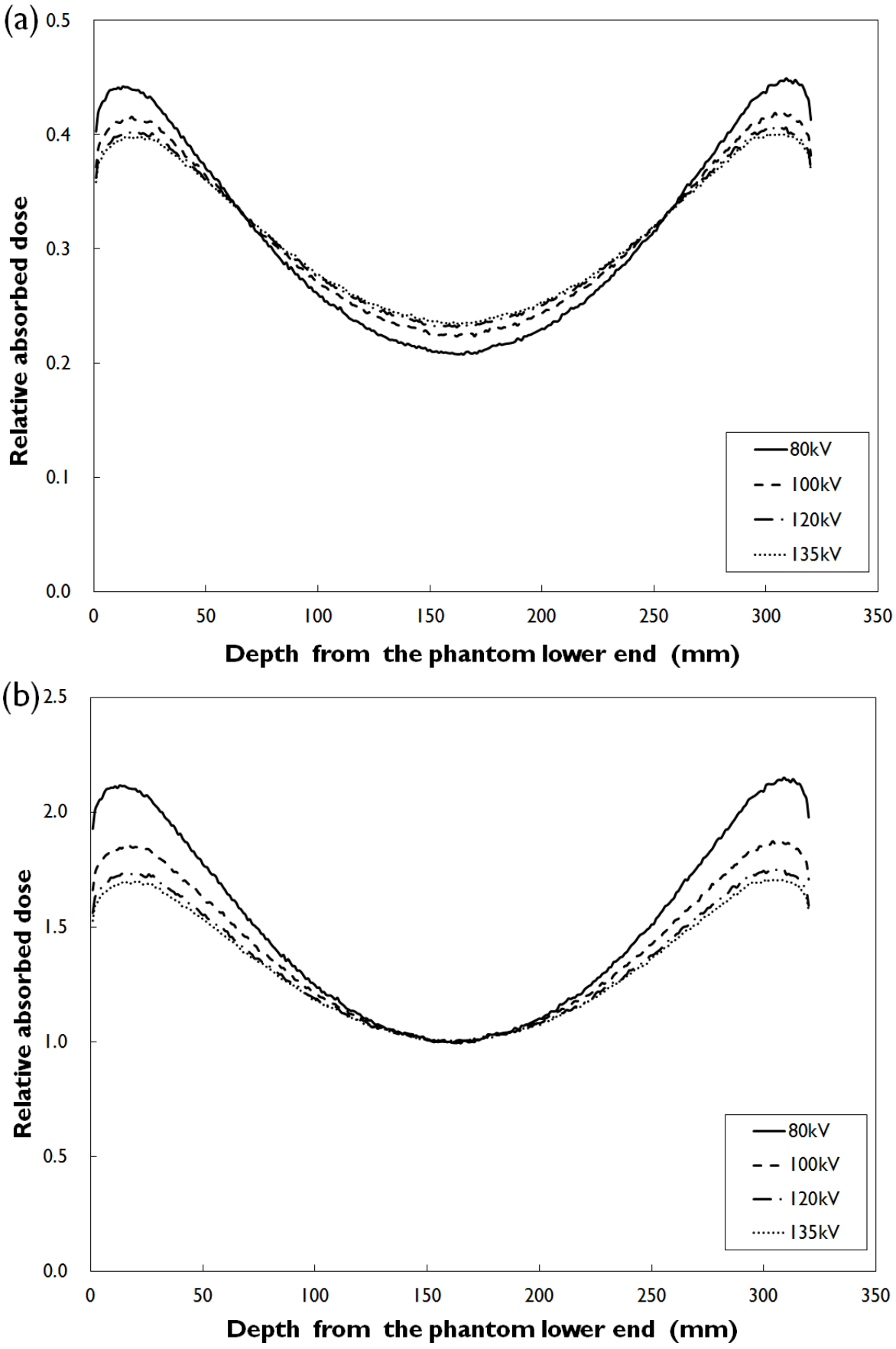

Fig. 5 Profiles of the total absorbed dose of primary and scattering x-ray components at each tube voltage. Each dose is normalized by (a) the total photon number and (b) the dose at the phantom center.

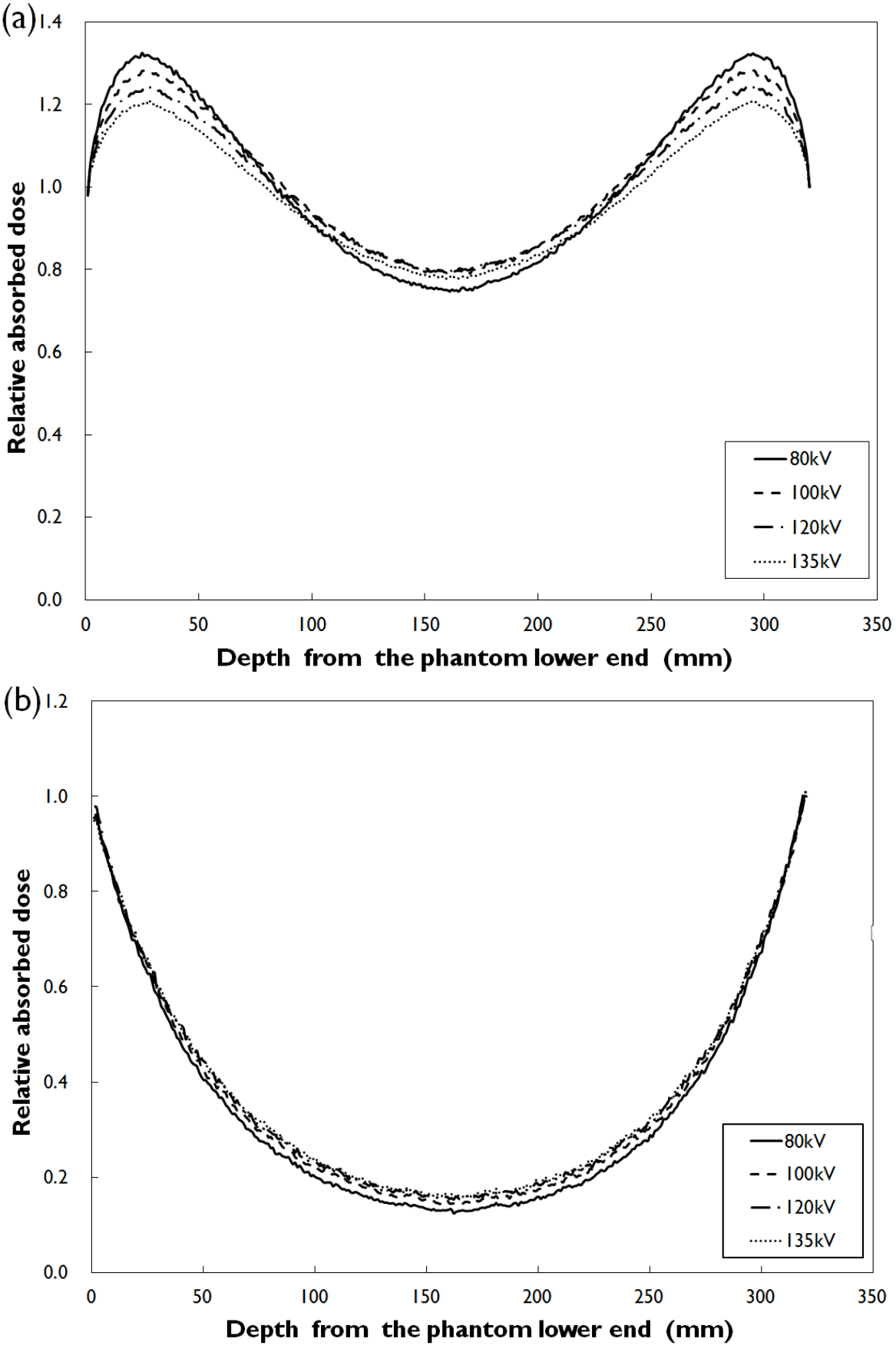

Fig. 6 Profiles of the absorbed dose caused by (a) the scattering x-ray and (b) the primary x-ray at each tube voltage.

Study of Monte Carlo dose calculation system aimed to clinical application

Y. Ishizawa[1], S. Dobashi[1], K. Sato[2], N. Kadoya[2], K. Ito[2], M. Chiba[2], K. Kishi[2] and K. Takeda[1]

[1]Health Science, Tohoku University Graduate School of Medicine, Sendai, 980-8574, Japan

[2]Tohoku University Hospital, Sendai, 980-8574, Japan

e-mail: ishizawa.rt@med .tohoku.ac.jp

Abstract

In clinical situation, Monte Carlo (MC) simulation is often used as a gold standard to evaluate and investigate the errors between dose calculation algorithms. However, it is cumbersome to input into the MC calculation system the patient geometry data and the irradiation parameters which vary in clinical situations. The aim of this study is to make the laborious setup for the clinical MC calculation easy. We developed a MC dose calculation system in which these setup parameters are automatically input from CT images and DICOM-RT files. We confirmed that this system properly realized the patient geometry and the irradiation beam arrangement by comparing a dose distribution calculated by this system with the one by a commercial treatment planning system (TPS). This system is a useful tool to make it easy to prepare for MC calculation in the clinical cases.

1. Introduction

Monte Carlo (MC) simulation is useful as a reference for dose calculation [1, 2] and requires the setting of the geometry and source information. It is important to prepare the information properly for an accurate MC calculation. However, in the clinical situation the setting for the MC calculation is cumbersome.

There are two reasons which make the setting for the clinical MC calculation difficult. The first reason is that the patient geometry has complex structure and many kinds of medium as compared to the simple phantom geometry such as a slab. The second reason is that the beam in clinical situation have many parameters such as the direction and the collimation in each irradiation field. It is desirable that such parameter setting can be performed easily.

To simplify the clinical MC simulation, we developed a MC dose calculation system in which input parameters are automatically prepared from CT images and DICOM-RT files for a given patient.

2. Materials and Methods

2.1 Setup for clinical MC calculation

To prepare for the clinical MC calculations, the CT images and the DICOM-RT files which include the radiotherapy planning data were used. These files were exported from a commercial treatment planning system (TPS) and converted to the patient geometry and the irradiation parameters for EGS5 calculation. The conversion process was performed automatically using MATLAB® (MathWorks, Natic, MA, USA). We extended EGS5 user code 'voxel user code' to fit the code for the clinical purpose.

A) CT-based patient geometry

Treatment planning CT data was used to obtain the information of the density and the medium of each patient. CT numbers were converted into density data by a Hounsfield unit to electron density conversion table. The conversion table should be specific to the CT device. In this study the following conversion formula given in ICRU Report 42 [3] were used to convert the CT number N_{CT} to the relative electron density ρ :

$$\rho = 1.0 + 0.001 \times N_{CT} \qquad (-1000 \leq N_{CT} \leq 100) \qquad (1)$$

$$\rho = 1.052 + 0.00048 \times N_{CT} \qquad (N_{CT} > 100) \qquad (2)$$

Medium constituting each voxel was determined according to the range of densities that are defined for each medium (Table 1). In this study the types of medium assigned to the geometry were air, lung, soft tissue, skeletal muscle, cartilage, and born cortex. The density and the elemental composition of each medium were defined in reference to ICRP Publication 23: the recommended elemental compositions [4]. Vacuum was assigned to the region outside the patient body.

B) Irradiation of therapeutic photon beam

EGS5 user code was extended to simulate the treatment beam by setting the irradiation direction and field. The configuration file for the MC calculation was produced by extracting the irradiation parameters (isocenter coordinate, gantry angle, couch angle, and collimator positions) from the DICOM-RT PLAN file exported from the TPS.

In the clinical situation, the irradiation direction is determined by the rotation of the gantry and couch for isocenter. We defined the direction of incident photon in MC calculation to produce the therapeutic beam by coordinate rotation of source position and direction cosine. The irradiation field was limited by jaw collimators and multi leaf collimators (MLCs). The beam collimation algorithm used in this study simply restricts photons to the light irradiation field at isocenter plane. Therefore the effect of MLC leaf end transmission and tongue and groove effects were not considered.

2.2 MC calculation in a clinical case

To confirm the validity of this system, a MC calculation for a patient of lung stereotactic body radiotherapy (SBRT) treated at Tohoku University Hospital was performed with this system. The MC calculated dose distribution was compared with the corresponding TPS result. The TPS dose were calculated in Varian Eclipse with analytical anisotropic algorithm (AAA) [5]. The commissioning of AAA was done for 6 MV photon beam from a Varian Clinac CL23EX accelerator (Varian Medical Systems, Palo Alto, Palo Alto, CA, USA). In the MC calculation, the energy spectrum and fluence of photon from this accelerator were determined by the optimization with pencil beam convolution (PBC) algorithm [6] so that the dose distribution calculated with PBC matches the measurement in water. The history was

set to 1×10^7 for each field. The energy cutoff parameters were set to be ECUT=0.521 MeV, PCUT=0.010 MeV. The dose calculation grid size was $2.5 \times 2.5 \times 2.5\ mm^3$. Seven-field treatment plan was created with the non-coplanar beams arranged by the gantry angle and the couch angle (Table 2).

3. Results

Figure 1 and Figure 2 show the dose distributions on a planar CT image calculated with EGS5 and TPS, respectively. Both results were normalized with the maximum dose of each dose distributions. The dose distributions along the beam path calculated by the MC calculation using this system was consistent with those by TPS.

Figure 3 shows the difference of the dose distribution between EGS5 and TPS. Remarkable discrepancies were observed around the edges of the irradiation fields, which reflects the fact that MC calculation properly reflects the extension of the range of the scattered electron in the low density region

4. Discussion

Since the dose distributions along the beam path matched between EGS5 and TPS, it was confirmed that the beam arrangement of MC calculation in this study properly reflected the clinical conditions.

The discrepancies in the field edges were caused by the difference in beam collimation model of the dose calculation algorithm. The beam collimation method of the MC calculation in this study was merely to restrict the photons from a point source to the light field shaped by the collimators. It is necessary to use the same beam collimation model with TPS for the precise comparison.

Additional reason for the discrepancies was using the different dose calculation algorithm and Hounsfield unit to electron density conversion table between EGS5 and TPS. Since the comparison of this study was based on visual evaluation of the dose distribution, the future issue is to compare the dose distribution by a quantitative evaluation.

5. Conclusions

We have developed a system to produce setup parameters for the EGS5 MC calculation in clinical condition automatically from CT Images and DICOM-RT files. We confirmed that out system successfuly produced a dose distribution which was consistent with the correspoinding dose distribution calculated by TPS. The system in the present study is useful tool as a basis of a framework that easily performs the clinical MC calculation.

References

1) Mark R. Arnfield, Christine Hartmann Siantar, Jeffrey Siebers, Pamela Garmon, Larry Cox, and Radhe Mohan, "The impact of electron transport on the accuracy of computed dose," Med. Phys. 27, 1266-1274 (2000).
2) Lasse Rye Aarup, Alan E. Nahum, Christina Zacharatou, Trine Juhler-Nottrup, Tommy Knoos, Hakan Nystron, Lena Specht, Elinore Wieslander, Stine S. Korreman, "The effect of different densities on the accuracy of various radiotherapy dose calculation methods: Implications for tumor coverage," Radiother. Oncol. 91, 405-414 (2009).
3) ICRU Report 42, "Use of computer in external beam radiotherapy procedures with high-energy photons and electrons," International Commission on Radiation Units and Measurements, Washington D.C. (1989).

4) ICRP Publication 23, "Report on the Task Group on Reference Man," SAGE Publications, CA (1975).
5) W Ulmer, J Pyyry, W Kissl, "A 3D photon superposition/ convolution algorithm and its foundation on results of Monte Carlo calculations," Phys. Med. Biol. 50 ,1767-1790 (2005)
6) A Ahnesjo, M Saxner, A Trepp, "A pencil beam model for photon dose calculation," Med. Phts. 19, 263-273 (1992)
7) Matthias Fippel, Freddy Haryanto, Oliver Dohm, Fridtjof Nusslin, "A virtual photon energy fluence model for Monte Carlo dose calculation," Med. Phys. 30, 301-311 (2003).

Element	$\rho_{\text{lower threshold}}$ (g/cm^3)	$\rho_{\text{upper threshold}}$ (g/cm^3)
Air	0.001	0.016
Lung	0.016	0.589
Adipose tissue	0.589	0.985
Muscle (skeletal)	0.985	1.074
Skeleton (cartilage)	1.074	1.35
Skeleton (cortical born)	1.35	

Table 1. The types of medium and its threshold (density) used for assignment to voxel.

Field number	1	2	3	4	5	6	7
Gantry angle	30°	330°	30°	330°	140°	180°	220°
Couch angle	40°	40°	320°	320°	0°	0°	0°

Table 2. The gantry angle and the couch angle used for the dose calculation in a clinical case.

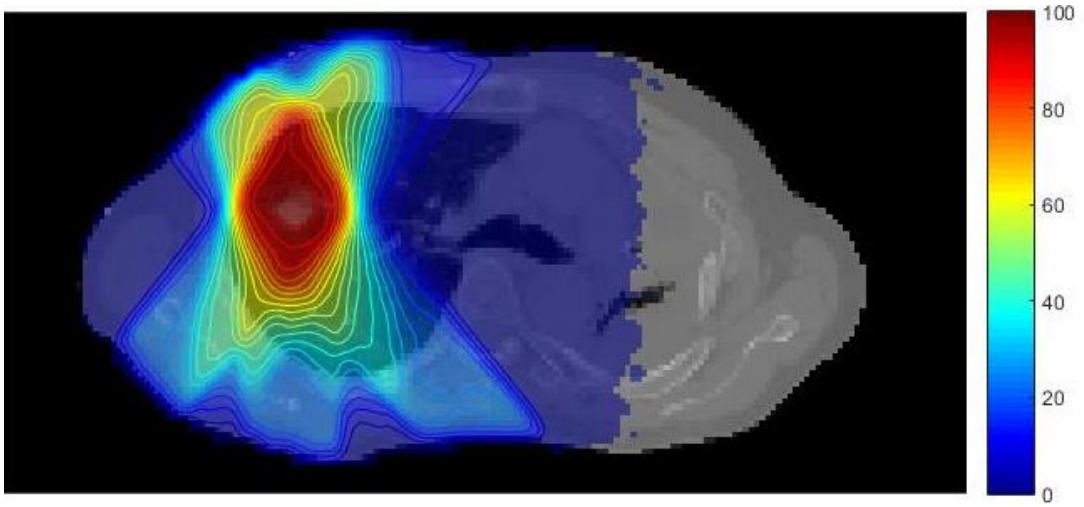

Figure 1. Calculated dose distribution using EGS5 with axial CT image.

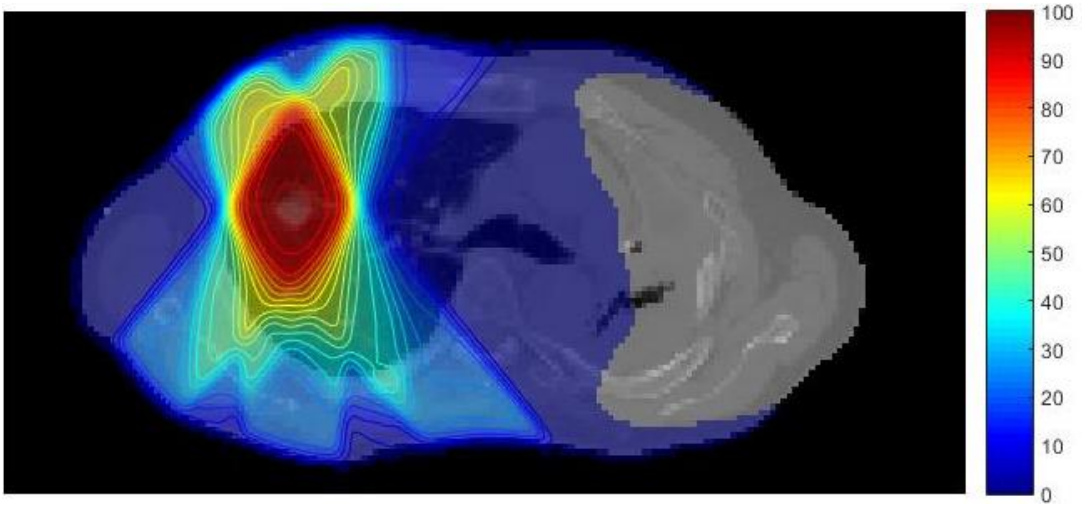

Figure 2. Calculated dose distribution using TPS with axial CT image.

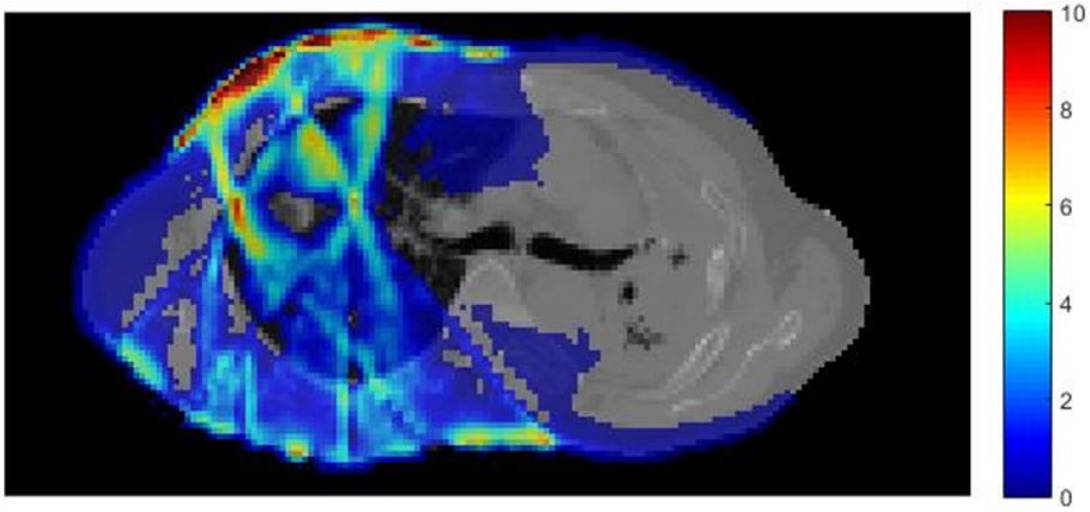

Figure 3. The difference of the dose distribution between EGS5 and TPS.

Monte Carlo simulation of the absorbed dose of air and Air-kerma strength by ^{192}Ir source

S. TSUJI, N. NARIHIRO[†‡] and M. OITA[‡]

Kawasaki Medical School, Kurashiki 701-0192, Japan

[†]*Kawasaki College of Allied Health Professions, Kurashiki 701-0194, Japan*

[‡]*Okayama University Graduate School of Health Sciences Division of Radiological Technology, Okayama 700-8558, Japan*

Abstract

Brachytherapy planning is performed based on the AAPM TG-43U1 protocol. The protocol is normalized in the air-kerma strength. The absorbed dose of air and the air-kerma are regarded as the same in a state where the charged particle equilibrium is established. However both dose not match within some distances from the radiation source. we investigate the air and air-kerma strength using EGS5 simulations. Determinations of the air-kerma strength are methods of using the mass energy-transfer coefficient and integrating the electron kinetic energy directly. These two results we were compared.

1 Introduction

Treatment planning systems of brachytherapy using an ^{192}Ir source perform calculations according to the American Association of Physicists in Medicine Task Group No 43 Updated Protocol (AAPM TG-43U1) [1]. AAPM TG-43U1 is following equation,

$$\dot{D}(r,\theta) = S_k \cdot \Lambda \cdot \frac{G(r,\theta)}{G(r_0,\theta_0)} \cdot g(r) \cdot F(r,\theta). \tag{1}$$

Parameters concerning the absolute values in this equation are the air-kerma strength S_k and the dose rate constant Λ. The air-kerma strength S_k is following equation,

$$S_k = \dot{K}(d) \cdot d^2, \tag{2}$$

here, $\dot{K}(d)$ is the air-kerma rate. The air-kerma strength dimension is U which defines 1U=1μGym^{2}h^{-1} =1cGycm^{2}h^{-1}. The dose rate constant Λ is following equation,

$$\Lambda = \frac{\dot{D}(r_0,\theta_0)}{S_k}, \tag{3}$$

here, $\dot{D}(r_0,\theta_0)$is the dose rate of the reference position (r_0,θ_0). Since the two constants can be determined by simulation, it can be calculated the absolute absorbed dose only in simulation.

2 Kerma and dose

The kama K is defined as follows,

$$K = \frac{\Delta E_{tr}}{\Delta m}, \tag{4}$$

here, Δm represents small mass of the target and ΔE_{tr} is the sum of the first kinetic energy imparted to the charged particles in the mass Δm. On the other hand, the absorbed dose D is expressed by the following equation,

$$D = \frac{\overline{\Delta E}}{\Delta m}, \tag{5}$$

here, $\overline{\Delta E}$ is the average energy imparted to the mass Δm. $K = D$ holds in a state where the charged particle equilibrium is established and photons enter the target mass with an energy less than 1 MeV [2].

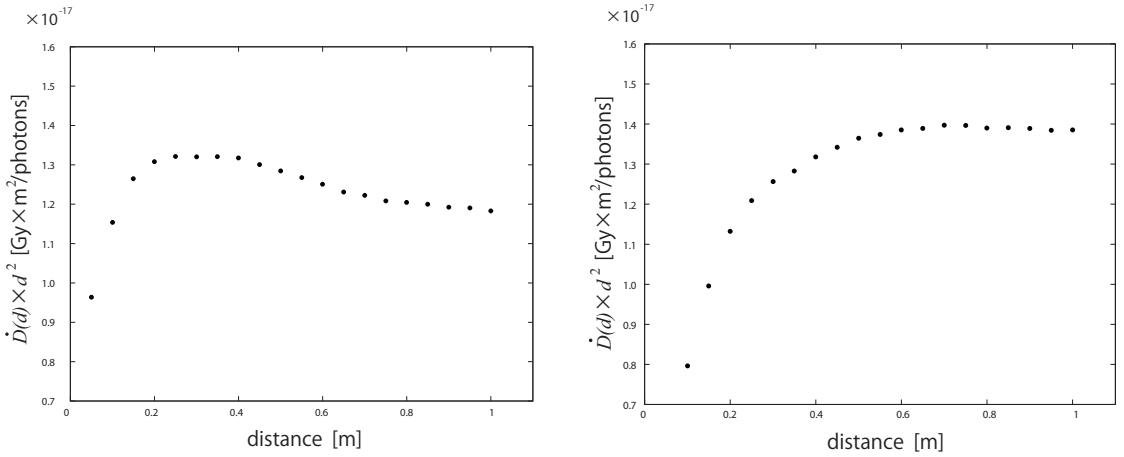

(a) (b)

Figure 1: The absorbed dose multiplied by the square of the distance in the air. The regions of the distance have a thickness of 1 mm shown as solid lines in Fig. 3. The source and detection areas are contained in a air sphere with a radius of 5 m. (All of the space is in the air.) (a): Radiation source: microSelectron HDR v2 in Fig. 2. The detected angle is $\pm 1°$ limited from the radiation source center in Fig. 2 or Fig. 3. (b): Radiation source: Point source. Detection solid angle area is 4π sr.

The absorbed dose multiplied by the square of the distance are shown in Fig. 1. Radiation sources in Fig. 1 are the microSelectron HDR v2 type shown in Fig. 2 (Figure 1(a)) and a point source without volume (Figure 1(b)). When using the microSelectron HDR v2 type, the measurement range is limited to $\pm 1°$ from the radiation source center as shown in Fig. 2 or Fig. 3. While the air-kerma strength should be constant without depending on distance, the absorbed dose multiplied by the square of the distance was not constant. It is considered that the charged particle equilibrium is not established within some distance from the source.

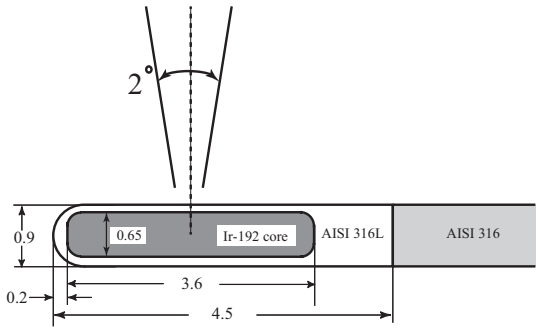

Figure 2: Mechanical design of a microSelectron HDR v2 ^{192}Ir source. A spread of the angle from the center of source shows the detection area.

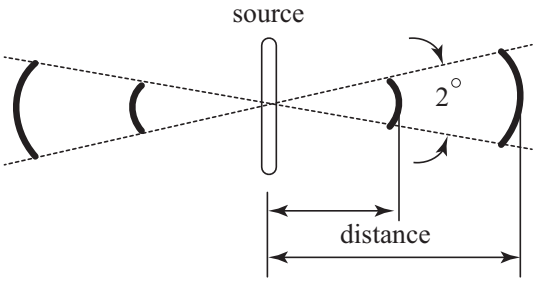

Figure 3: The relationship between the source and detection areas. Solid lines show detection areas which is limited to $\pm 1^\circ$ and 1 mm thickness. The detection areas are in the air and the other regions are air or vacuum. The source and detection areas are contained in a sphere with a radius of 5 m.

3 Air-kerma strength using a table

Equation (4) can be expressed as follows using the mass energy-transfer coefficient,

$$K = \int E\phi(E) \left(\frac{\mu_{tr}}{\rho} \right) dE, \tag{6}$$

where E, $\phi(E)$ and (μ_{tr}/ρ) are the photon energy, the energy fluence per unit energy interval and the mass energy-transfer coefficient [2, 3, 4, 5]. The mass energy-transfer coefficients are listed in the table [2, 6]. Fig 4 shows the air-kerma rate $\dot{K}(d)$ adapted the mass energy-transfer coefficient multiplied by the square of the transverse distance d using equation (6).

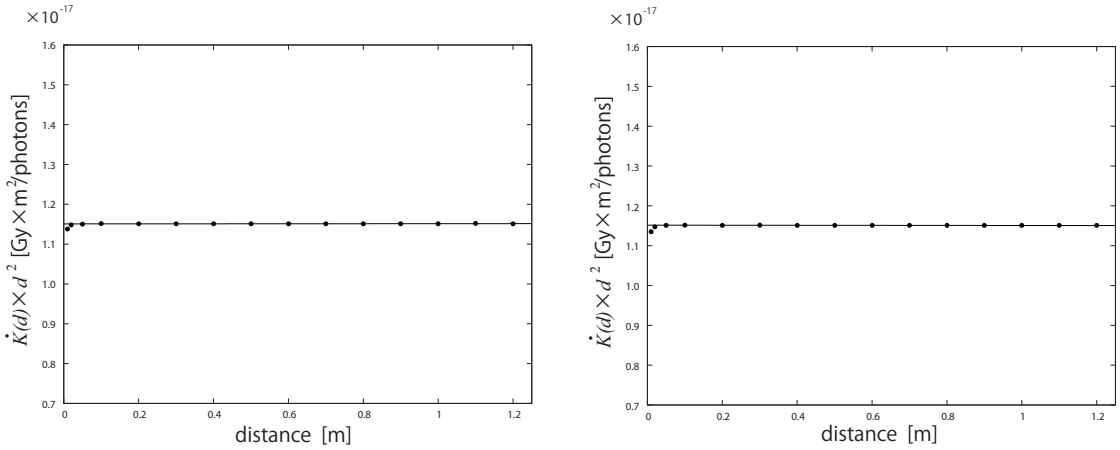

(a) (b)

Figure 4: The air-kerma rate adapted the mass energy-transfer coefficient multiplied by the square of the transverse distance in a sphere with a radius of 5 m. The mass energy-transfer coefficients are listed in the tables [2, 6]. The detection areas and the angular limitation are shown in Fig. 3. The solid lines are linear function fits, except the first one point($x = 0.01$(m)). (a): All of space is in the air. (b): The detection areas are in the air and the other area is in a vacuum.

Fig 4 (a) is the result in a sphere with a radius of 5 m filled with air and Fig 4 (b) is the vacuum of the sphere without the target regions. Air-kerma strength S_k is the air-kerma rate $\dot{K}(d)$ *in vacuo* multiplied by the square of the transverse distance d from the source,

$$S_k = \dot{K}(d) \cdot d^2. \tag{7}$$

The deviation of $\dot{K}(d)$ from inverse-square law is due to the buildup of scattered photons in air [7, 8]. Therefore, it becomes as follows in air,

$$\dot{K}(d) \cdot d^2 = S_k + \alpha \cdot d. \tag{8}$$

To determine the air-kerma strength S_k, Intercepts ($= S_k$) are obtained fitting with a linear function.

$$S_k = (1.1501 \pm 0.0004) \times 10^{-17} \quad [\mathrm{Gym}^2/\mathrm{photons}] \quad \text{(in the air)}, \tag{9}$$
$$S_k = (1.1504 \pm 0.0005) \times 10^{-17} \quad [\mathrm{Gym}^2/\mathrm{photons}] \quad \text{(in a vacume)}. \tag{10}$$

History number for determining the equation (9) or (10) is 10^8.

4 Air-kerma strength obtained directly

While the air-kerma strength was obtained air-kerma strength using the table [2, 6] in Section 3, the Monte Carlo simulation should be able to directly determine the air-kerma strength. According to Equation (4), we integrate the electron kinetic energy immediately after the photon reactions in the region. In EGS5, when photoelectric absorption, the Compton scattering and electron pair production occur in the target, the electron kinetic energy is scored. In main program, it is necessary to flag as follows.

```
!   Set iausfl for photon reaction to create cahrged particle
      iausfl(17)=1   ! after pair
      iausfl(19)=1   ! after Compt
      iausfl(21)=1   ! after Photo
```

In ausgab subroutine program, we check which `np` related electrons after the reactions `iarg=16`, `iarg=18` and `iarg=20`. The directly calculated air-kerma rate $\dot{K}(d)$ multiplied by the square of

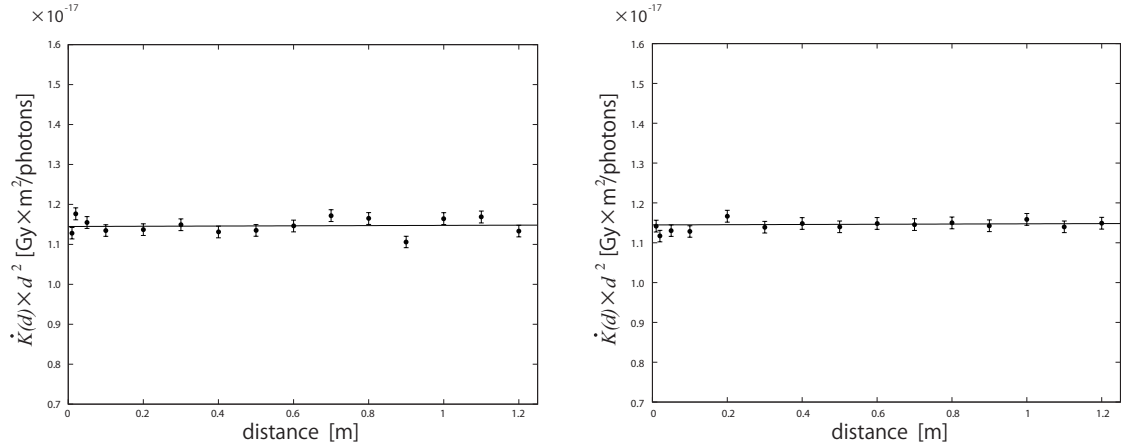

(a) (b)

Figure 5: The directly calculated air-kerma rate multiplied by the square of the transverse distance in a sphere with a radius of 5 m. The electron kinetic energies in the regions are integrated in the Monte Carlo simulation. The detection areas and the angular limitation are shown in Fig. 3. The solid lines are linear function fits. (a): All of space is in the air. (b): The detection areas are in the air and the other area is in a vacuum.

the transverse distance d are shown in Fig. 5. Fig 5 (a) is the result in a sphere filled with air and

Fig 5 (b) is the vacuum of the sphere without the target regions. As in Section 3, the air-kerma strength S_k is follows,

$$S_k = (1.1447 \pm 0.0088) \times 10^{-17} \ [\mathrm{Gym}^2/\mathrm{photons}] \quad \text{(in the air)}, \tag{11}$$

$$S_k = (1.1448 \pm 0.0088) \times 10^{-17} \ [\mathrm{Gym}^2/\mathrm{photons}] \quad \text{(in a vacume)}. \tag{12}$$

History number for determining the equation (11) or (12) is 6×10^{10}.

5 Conclusion

The consensus value of dose rate constant of microselectron HDR v2 type ${}_{CON}\Lambda$ is listed as follows [9],

$${}_{CON}\Lambda = (1.109 \pm 0.012) \ \mathrm{cGy} \cdot \mathrm{h}^{-1} \cdot \mathrm{U}^{-1}.$$

In Equation (3), the dose rate constant Λ is obtained by dividing the absorbed dose $D(r_0, \theta_0)$ in water at the reference position with the air-kerma strength S_k. If unambiguous method of determining such as the air-kerma strength using the mass energy-transfer coefficient table [3, 4, 5], deviations of absorbed dose coefficient do not much spread in each experiment. Dose rate constant should be published as a consensus data averaging those with the consideration of how to determine the air-kerma strength. In our results, we obtained the air-kerma strength in a vacuum,

$$S_k = (1.1504 \pm 0.0005) \times 10^{-17} \ [\mathrm{Gym}^2/\mathrm{photons}],$$

using the mass energy-transfer coefficient table and,

$$S_k = (1.1448 \pm 0.0088) \times 10^{-17} \ [\mathrm{Gym}^2/\mathrm{photons}],$$

with a directly calculation. Both were consistent within the error.

6 Acknowledgements

We are deeply grateful to Prof. Hirayama. He gives insightful comments and made enormous contribution to make the ausgab subroutine directly calculating the electron kinetic energy after the photon reactions. The computations were mainly carried out using the computer facilities at the Research Institute for Information Technology, Kyushu University.

References

[1] M. J. Rivard, B. M. Coursey, L. A. DeWerd, W. F. Hanson, M. S. Huq, G. S. Ibbott, M. G. Mitch, R. Nath, and J. F. Williamson, "Update of AAPM Task Group No.43 Report: A revised AAPM protcol for brachytherapy dose calculations," Med. Phys. **31**,633-673 (2004).

[2] H. Hirayama, "Concepts of Dose for Photons and Relations between Conversion Factor to Effective Dose -At the Enforcement of Regulation Based on 1990 ICRP Recomendation," Nihon-Genshiryoku-Gakkai Shi (J. At. Energy Soc. Jpn.) **43**, 427-432 (2001). [in Japanese].

[3] T. P. Selvam, K. N. G. Rajan, P. S. Nagarajan, P. Sethulakshmi and B. C. Bhatt,"Monte Carlo aided room scatter studies in the primary air kerma strength standardization of a remote afterloading ^{192}Ir HDR source," Phys. Med. Biol. **46**, 2299-2315 (2001).

[4] M. J. Rivard, D. Granero, J. Perez-Calatayud and F. Ballester, "Influence of photon energy spectra from brachytherapy sources on Monte Carlo simulations of kerma and dose rates in water and air," Med. Phys. **37**,869-875 (2010).

[5] J. Borg and D. W. O. Rogersa, "Spectra and air-kerma strength for encapsulated ^{192}Ir sources," Med. Phys. **26**, 2441-2444 (1999).

[6] National Institute of Standards and Technology, http://physics.nist.gov/PhysRefData/XrayMassCoef/tab3.html, or http://physics.nist.gov/PhysRefData/XrayMassCoef/tab4.html

[7] G. M. Daskalov, E. Löffler, and J. F. Williamson, "Monte Carlo-asided dosimetry of new high dose-rate brachytherapy source," Med. Phys. **25**, 2200-2208 (1998).

[8] F. Ballester, J. Pérez-Calatayud, V. Puchades, J. L. Lluch, M. A. Serrano-Andrés, Y. Limami, F. Lliso, and E. Casal, "Monte Carlo dosimetry of the Buchler high dose rate ^{192}Ir source," Phys. Med. Biol. **46**, N79-N90 (2001).

[9] J. Perez-Calatayud, F. Ballester, R. K. Das, L. A. Dewerd, G. S. Ibott, A. S. Meigooni, Z. O. Ouhib, M. J. Riverd, R. S. Sloboda, J. F. Williamson, "Dose calculation for photon-emitting brachytherapy sources with average energy higher than 50keV: Report of the AAPM and ESTRO," Med. Phys. **39**, 2904-2929 (2012)

BENCHMARK ANALYSIS OF ABSORBED DOSE RATE FOR $^{90}Sr/^{90}Y$ BETA RADIATION

S. Iwai, F. Nobuhara

Department of Engineering, Tokyo Nuclear Services Co., Ltd.,
1-3-5, Taito, Taito-ku, Tokyo 110-0016, Japan
e-mail: iwai@tokyo-nucl.co.jp

Abstract

In the radiation shielding field, the absorbed dose for gamma radiation has mainly been evaluated, while the external absorbed dose for beta radiation has sometimes not been considered up to the present time. However, after the Fukushima Nuclear Accident in 2011, needs for evaluation of the absorbed dose from distant accumulated beta nuclides has been increasing. Therefore, we focused on the beta sources $^{90}Sr/^{90}Y$ released in the accident and performed benchmark analysis using Electron Gamma Shower code version 5 (EGS5) for the evaluation of the absorbed dose for beta radiation. The results of simulation were in good agreement with the measured results to within 9% in the range of 1 to 1000μm depth in ICRU tissue. It has been verified that EGS5 code provides accurate evaluation of absorbed dose for external beta radiation.

1. Introduction

In the radiation shielding field, the absorbed dose for gamma radiation has mainly been evaluated in gamma heating, hydrogen generation and so on, because of its higher permeability to a material compared to beta radiation, while that for beta radiation has sometimes not been considered up to the present time. However, after the Fukushima Nuclear Accident in 2011, considerable amount of beta emitters has been accumulated in one place, and needs for evaluation of absorbed dose from accumulated beta nuclides has been increasing. Therefore, we focused on the beta sources $^{90}Sr/^{90}Y$ released in the accident and performed benchmark analysis using Electron Gamma Shower code version 5 (EGS5) [1] for the evaluation of the absorbed dose for beta radiation.

2. Materials and methods

2.1 Benchmark method

We performed the benchmark analysis on the basis of the experimental conditions by Physikalisch-Technische Bundesanstalt (PTB) to measure the absorbed dose rate in ICRU tissue phantom. We simulated the experiment to evaluate absorbed dose rate for $^{90}Sr/^{90}Y$ radiation using EGS5 and compared the simulated value with the measured data. The results of the measurement are described in PTB reports [2] [3] [4], and a part of these report is cited in "JIS Z 4514:2010" [5] as a reference. PTB is the national metrology institute of Germany and provides a unit of absorbed dose rate of beta radiation to tissue as a national standard.

2.2 Measurement by PTB

The measurement system developed by PTB consisted of irradiation devices, a source holder, a source stand, a

beam-flattening filter, a phantom, an extrapolation ion chamber and so on. In the experiment, the absorbed dose rates were measured for 3 irradiation devices. As a result of the measurement, the absorbed dose rate at depth d in the phantom for beta radiation can be approximated by the following fitting function (1).

$$T(d) = \frac{\sum_{i=0}^{8} \left(T_i \cdot \cos\left[i \cdot \arccos\{X(d)\} \right] \right) - \tau_{br}}{1 - \tau_{br}} \quad with \quad X(d) = 2 \cdot \frac{\log_{10}\left(\frac{d + d_{shift}}{d_{\min} + d_{shift}} \right)}{\log_{10}\left(\frac{d_{\max} + d_{shift}}{d_{\min} + d_{shift}} \right)} - 1 . \qquad (1)$$

Source-specific parameters of function *T(d)* are shown in the PTB reports. We performed the benchmark analysis by comparing the simulated values with the measured results using the above fitting function (1).

2.3 Simulation using EGS5

Figure 1 shows a calculation geometry modeled from the PTB reports. The $^{90}Sr/^{90}Y$ source with the nominal activity of 460MBq in each nuclide was in a source capsule with a source window having 79mg/cm^2 thickness. The source holder was not considered in our simulation since the size of the source holder was not described in the PTB reports. The beam-flattening filter was mounted at 10cm distance from the source holder, and the ICRU tissue phantom was mounted at 11cm, 30cm and 50cm distances from the source holder. We set stratified tally regions at the source-side surface in the phantom and each of the stratum of tally regions was set to 30mm in diameter, 2μm in thickness. In table 1, the materials used and their properties are listed.

In the simulation, we used $^{90}Sr/^{90}Y$ beta source spectrum given in ICRP Pub.107 [6]. The absorbed dose rate for beta radiation was evaluated using cumulative deposit energy, and that for bremsstrahlung was evaluated by multiplying gamma flux with mass energy-absorption coefficients for ICRU tissue [7]. In addition, electrons and photons were followed down to 1 keV, and the number of histories to run was set to 1×10^9 so that an error of the evaluation value would become less than 1%. In our actual cases, errors of the evaluation values in the following results for beta radiation were less than 1%.

3. Results

3.1 Without beam-flattening filter

Figure 2(a) shows a comparison of the simulated and the measured results of absorbed dose rates for beta radiation at 11cm, 30cm and 50cm distances from the source holder without the beam-flattening filter, and Figure 2(b) shows the similar comparison for beta radiation and bremsstrahlung on the logarithmic ordinate. In the comparison for beta radiation, the simulated absorbed dose rates agreed with the measured absorbed dose rates to within 9% in the range of 1 to 1000μm depth in ICRU tissue. It was considered that the differences between the simulated and the measured results were very small even though the calculation geometry did not perfectly emulate the measurement system. In case of bremsstrahlung, the simulated absorbed dose rates were consistent with the measured absorbed dose rates (approximately within 30%).

3.2 With beam-flattening filter

Figure 3(a) shows a comparison of the simulated and the measured results of absorbed dose rates for beta radiation at 30cm distance from the source holder with and without the beam-flattening filter, and Figure 3(b) shows the similar comparison for beta radiation and bremsstrahlung on the logarithmic ordinate. In the comparison, the simulated absorbed dose rates for beta radiation agreed with the measured absorbed dose rates to within 3% in the same range for the without-filter case, and that for bremsstrahlung agreed with the measured absorbed dose rates to within 10%.

4. Conclusions

In our benchmark analysis, we simulated the PTB experiment to evaluate absorbed dose rate for $^{90}Sr/^{90}Y$ radiation using EGS5 code and compared the simulated results with the measured results. The results of simulation were in good agreement with the measured results to within 9% in the range of 1 to 1000μm depth in ICRU tissue. It has been verified that EGS5 code provides accurate evaluation of absorbed dose for external beta radiation.

Acknowledgment

We are grateful to Dr. Morihito Shimizu, National Metrology Institute of Japan, for providing EGS5-MPI [8] used for the simulation.

References

1) H. Hirayama, Y. Namito, A. F. Bielajew, S. J. Wilderman, and W. R. Nelson, "THE EGS5 CODE SYSTEM," SLAC-R-730 (2005).
2) P. Ambrosi, G. Buchholz and K. Helmstädter, "The PTB Beta Secondary Standard BSS2 for radiation protection," 2007 JINST 2 P11002.
3) R. Behrens, G. Buchholz, "Extensions to the Beta Secondary Standard BSS2 Consolidated version from www.ptb.de," (2012).
4) Jens Brunzendorf, "Depth-Dose Curves of the Beta Reference Fields 147Pm, 85Kr and 90Sr/90Y Produced by the Beta Secondary Standard BSS2," 2012 Radiation Protection Dosimetry.
5) JIS Z 4514:2010, "Calibration of absorbed dose to tissue meters and dose equivalent meters and the determination of their response as a function of beta radiation energy and angle of incidence," (2010).
6) ICRP Publication 107, "Nuclear Decay Data for Dosimetric Calculations," Annals of the ICRP, vol.38, No.3, 2008.
7) J. H. Hubbell and S. M. Seltzer, "Tables of X-Ray Mass Attenuation Coefficients and Mass Energy-Absorption Coefficients from 1 keV to 20 MeV for Elements Z =1 to 92 and 48 Additional Substances of Dosimetric Interest," Radiation Physics Division, PML, National Institute of Standards and Technology (NIST).
8) M. Shimizu, National Metrology Institute of Japan, "EGS5-MPI user's manual," (2013).

Table 1. Density and composition of materials used in the simulation

Material	Air	ICRU tissue	PET	SUS	$SrCO_3$
Density (g/cm^3)	$1.1974 \cdot 10^{-3}$	1.0	1.38	8.06	3.76
Composition (wt.%)					
H		10.12	4.2		
C	0.01	11.1	62.5	0.1	8.14
N	75.53	2.6			
O	23.18	76.18	33.3		32.51
Si				0.7	
Ar	1.28				
Cr				18	
Mn				1	
Fe				71.2	
Ni				9	
Sr					59.35

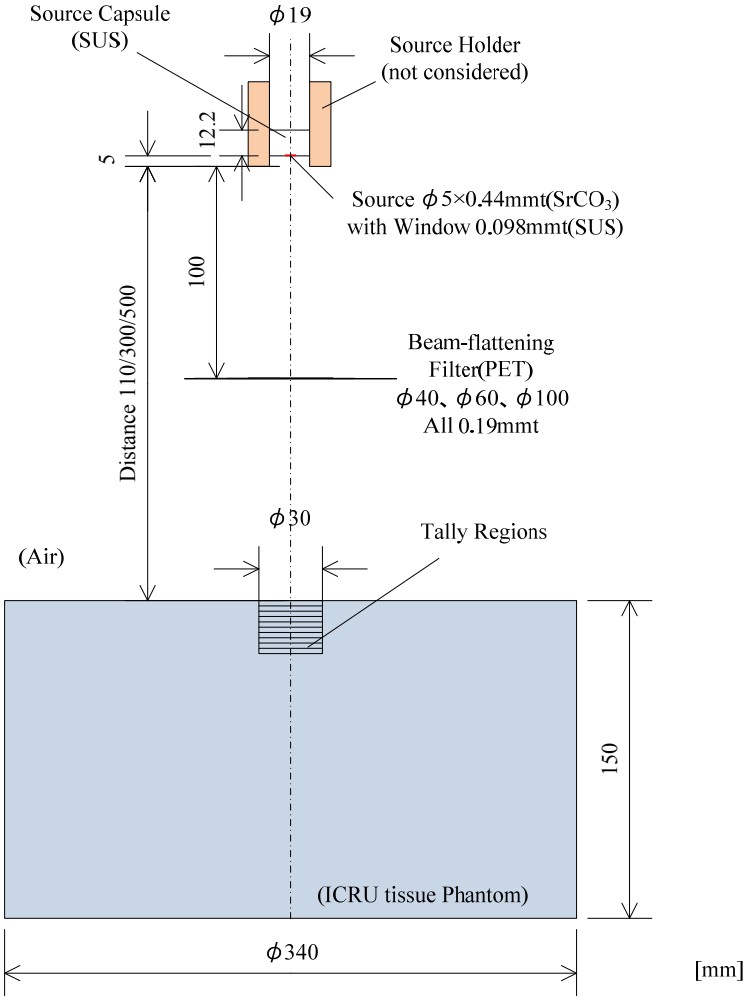

Figure 1. Calculation geometry of benchmark analysis.

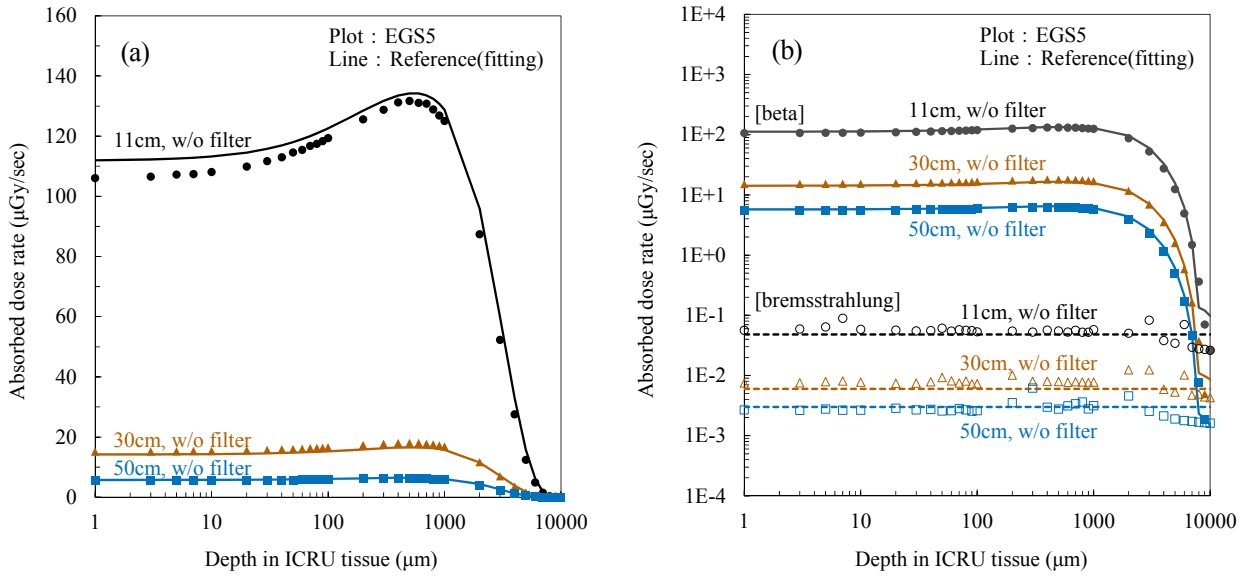

Figure 2. Comparison of simulated and measured absorbed dose rates to tissue for beta radiation and bremsstrahlung *without beam-flattening filter* at 11cm, 30cm and 50cm distances between source holder and ICRU tissue phantom: (a) linear ordinate; (b) logarithmic ordinate.

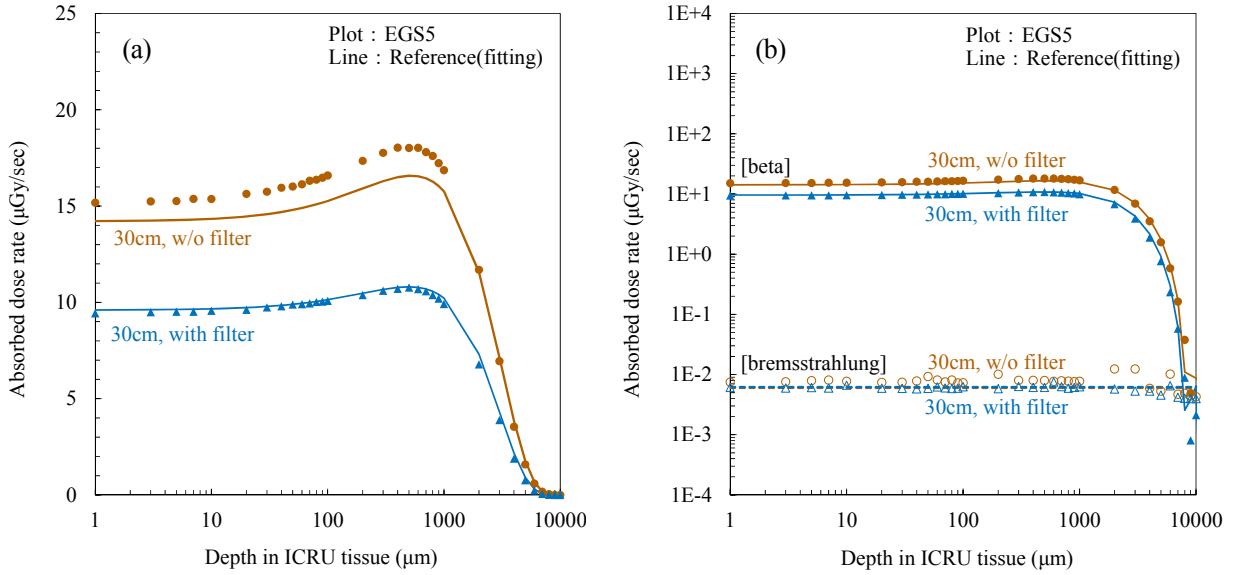

Figure 3. Comparison of simulated and measured absorbed dose rates to tissue for beta radiation and bremsstrahlung *with/without beam-flattening filter* at 30cm distance between source holder and ICRU tissue phantom: (a) linear ordinate; (b) logarithmic ordinate.

EVALUATION OF CS-137 ORIENTED INTERNAL RADIATION DOSE IN APODEMUS WHICH CAPTURED IN DIFFICULT-TO-RETURN ZONE AROUND FUKUSHIMA DAIICHI NUCLEAR POWER STATION

D. Endoh*[1], H. Hirayama[2], H. Ishiniwa[3], T. Okano[3], M. Onuma[3]

[1] Department of Radiation Biology, School of Veterinary Medicine, Rakuno Gakuen University, Ebetsu 069-8501, Japan

[2] Radiation Science Center, KEK, High Energy Accelerator Research Organization, Tsukuba 305-0801, Japan

[3] Ecological Genetics Analysis Section, Center for Environmental Biology and Ecosystem, National Institute for Environmental Studies, Tsukuba, 305–8506, Japan

E-mail of corresponding author: dendoh@rakuno.ac.jp

1. Introduction

After accident of Fukushima Daiichi Nuclear Power Station (FDNPS), a large amount of radionuclides was emitted into the surrounding environment. Tanaka et al. [1] showed that more than 76% of the radionuclides were retained within 5 cm of the surface. At the early time after the accident, Imanaka et al [2] estimated radionucleotide concentration in 5-cm soil is 10 to 43 kBq/kg^{-1} at 5 different points. These data suggested that wild life animals may expose significant dose. Radiation dose calculated from soil and seawater radionucleotide concentration suggested to affect lifespan and reproductive success of wildlife animals in 2011[3]. In 2012 to 2014, major factor of radiation dose changed from ^{131}I to radioactive cesium, thus influences of radionucleotide should be re-estimated according to radioactivity of ^{137}Cs. In this study, we estimated internal radiation dose in testis of *Apodermas speciosus* which is the large Japanese field mouse.

2. Materials and Methods

2.1 Sampling and estimation of radioactivity

The large Japanese field mouse was captured in difficult-to-return zone around (FDNPS), in 2012, 2013 and 2014. The mouse was autopsied after euthanasia and testis were corrected for measurement of radioactivity. Frequency and energy of gamma-rays were measured by germanium semiconductor detector.

2.2 Estimation of radiation dose per intra-testis ^{137}Cs

Energy spectrum of ^{137}Cs beta-ray was calculated by software made by Hideki Kato

(http://www.fujita-hu.ac.jp/~hid-kato/freesoft.html) which referring formula for energy distribution[4]. Energy deposition of beta-particles generated from ^{137}Cs were calculated with the Monte Carlo electron-photon transport code EGS5[5]. Absorbed radiation dose in testis was calculated from summation of energy depositions ellipsoid which is similar to testis. Materials of testis and surrounding tissues were assumed to soft tissue (testis) and adipose tissue (tissue surrounding testis).

3. Results and discussion

Radioactivity concentration were measured on whole body of the mouse. Average value for radioactivity concentration in 2012 -2014 were listed in Table 1.

Table 1

Year for sampling	Average radioactivity concentration of ^{137}Cs in testis (Bq/kg)
2012	35,518
2013	3,904
2014	16,494

Contribution of beta-ray from adipose tissue was estimated to be low from Monte Carlo calculations of radiation absorbed dose assuming various sizes of soft tissues (Fig. 1)

Figure 1

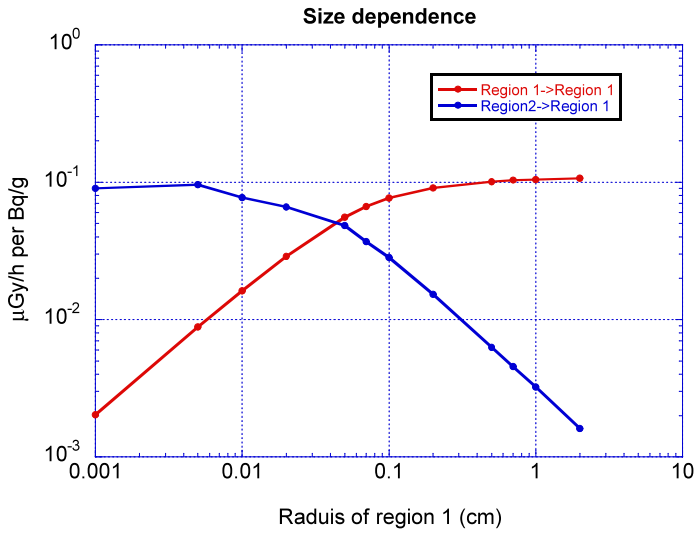

(Figure Caption) Contribution of ^{137}Cs in testis-surrounding tissues to absorbed dose of

testis. Shape of testis was assumed to ellipsoid (Region 1) and surrounding adipose tissue assumed to Region2.

From Monte Carlo simulations, beta-ray from surrounding tissue was very low if testis size was greater than 0.5 cm. Thus, radiation dose should be calculated from beta-ray inner ellipsoid simulating testis since most of testis were measured larger than 0.5 cm.

From assumptions above, 137Cs-internal absorption dose of tissue was calculated to 0.1015 μGy/h per Bq/g. Average absorbed dose were listed in Table 2.

Table 2

Year for sampling	Calculated absorbed dose from ^{137}Cs-beta ray in testis (μGy/h)
2012	3.60
2013	0.40
2014	1.67

Acknowledgments

References

[1] K. Tanaka, Y. Takahashi, A. Sakaguchi, M. Umeo, S. Hayakawa, H. Tanida, T. Saito, and Y. Kanai, "Vertical profiles of iodine-131 and cesium-137 in soils in Fukushima prefecture related to the Fukushima Daiichi Nuclear Power Station accident," *Geochem. J.*, vol. 46, no. 1, pp. 73–76, 2012.

[2] T. Imanaka, S. Endo, and M. Sugai, "Early radiation survey of Iitate village, which was heavily contaminated by the Fukushima Daiichi accident, conducted on 28 and 29 March 2011," *Heal. …*, 2012.

[3] J. Garnier-Laplace, K. Beaugelin-Seiller, and T. G. Hinton, "Fukushima wildlife dose reconstruction signals ecological consequences," *Environ. Sci. Technol.*, vol. 45, no. 12, pp. 5077–5078, 2011.

[4] H. Daniel, "Shapes of beta-ray spectra," *Rev. Mod. Phys.*, vol. 40, no. 3, p. 659, 1968.

[5] H. Hirayama, Y. Namito, W. R. Nelson, A. F. Bielajew, S. J. Wilderman, and U. Michigan, “The EGS5 code system,” United States. Department of Energy, 2005.